

## CHAPTER THREE

# 2D Boron Nitride: Synthesis and Applications

G.R. Bhimanapati<sup>\*,†</sup>, N.R. Glavin<sup>‡</sup>, J.A. Robinson<sup>\*‡,1</sup>

<sup>\*</sup>The Center for 2-Dimensional and Layered Materials, The Pennsylvania State University, University Park, PA, United States

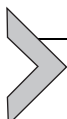
<sup>†</sup>NSF I/UCRC Center for Atomically Thin Multifunctional Coatings, The Pennsylvania State University, University Park, PA, United States

<sup>‡</sup>Air Force Research Laboratory, Wright Patterson AFB, Dayton, OH, United States

<sup>1</sup>Corresponding author: e-mail address: jrobinson@psu.edu

## Contents

1. Introduction	101
2. Structure and Properties of 2D Boron Nitride	103
2.1 Structural Properties	103
2.2 Thermal Stability	105
3. Synthesis of BNNS	107
3.1 Mechanical Exfoliation	108
3.2 Solvent-Assisted Ultrasonication	110
3.3 Acid Exfoliation	113
3.4 Chemical Functionalization of h-BN	113
3.5 Unzipping of BNNTs	118
3.6 Single and Few-Layer h-BN via CVD	120
3.7 Defect Manipulation in h-BN Using Scanning Tunneling Microscopy	127
4. Applications for 2D h-BN Atomic Layers	128
4.1 Dielectrics in Next-Generation Nanoelectronic Devices	128
4.2 Vertical Tunneling Device and Behavior	131
4.3 h-BN in Protective Coatings	133
4.4 h-BN in Gas Sensing	135
4.5 h-BN as Filler for Binder-Free Anode for Lithium Ion Batteries	136
4.6 Hyperbolicity in h-BN	137
References	139



## 1. INTRODUCTION

Boron nitride (BN) is a chemical compound that is isoelectronic and isostructural to carbon with equal composition of boron and nitrogen atoms. The first synthesis of boron nitride was in 1842 by [Balmain \(1842\)](#) using

molten boric acid and potassium cyanide; however, stabilizing the material to form powders was a challenge until recently ([Anon, 1958](#)). Similar to carbon, boron nitride is produced in amorphous and crystalline forms. In its crystalline form, boron nitride exists in three major allotropes: hexagonal boron nitride (h-BN) resembling graphite ([Fig. 1A](#)), sphalerite boron nitride ( $\beta$ -BN) resembling cubic diamond, and wurtzite boron nitride ( $\gamma$ -BN) resembling hexagonal diamond form ([Pakdel et al., 2014](#)). Unlike the carbon fullerenes ( $C_{60}$  bulky balls), BN fullerenes have mostly squares or octagons instead of pentagons to avoid the thermodynamically unfavorable B–B and N–N bonding ([Fig. 1D](#)). Similar to 1D carbon nanotubes (CNTs), BN nanotubes (BNNTs) ([Fig. 1C](#)) also exist which are isoelectric to CNTs in terms of chirality, tube diameters, and number of walls. Out of these different phases, h-BN is the most common stable form of BN and most of the interest started after the isolation of graphene sheets in 2004 ([Bhimanapati et al., 2015](#)). h-BN is also a layered structure and within each layer, the boron and nitrogen atoms are bound by strong covalent bonds in-plane and each layer is held together by van der Waals forces. A single layer of h-BN is typically referred as a BN nanosheet or BNNS. This nomenclature is only true for h-BN sheets whose aspect ratio is small. For higher aspect ratio materials where the typical widths will be  $<50$  nm, they are referred as BN nanoribbons or BNNR's.

Although h-BN has a similar structure to graphene, it is a wide bandgap material with an intrinsic band gap ( $E_g$ ) of 5.9 eV when compared to the highly conductive graphene. It is also thermally conductive, which is attractive for many electronic applications since it can be used as electrically

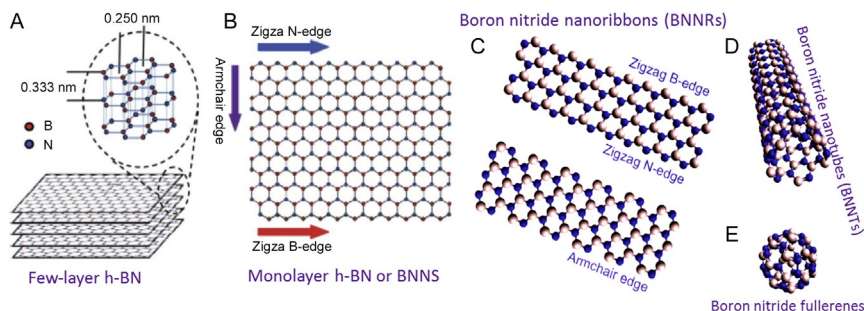


**Fig. 1** Boron nitride allotropes: (A) few-layer hBN, (B) monolayer h-BN nanosheet or BNNS, (C) boron nitride nanoribbons (BNNRs) with different edge termination leading to zigzag B-edge and armchair edge structures, (D) boron nitride nanotubes (BNNT), and (E) BN fullerenes ([Lin and Connell, 2012](#); [Pakdel et al., 2014](#)).

insulating filler material for polymer or ceramic composites (Ghosh et al., 2008; Yurdakul et al., 2012), thermal radiators (Song et al., 2012; Zhi et al., 2009), field emitters (Chen et al., 2008a), and UV emitters (Golberg et al., 2010; Zhi et al., 2005). In addition to its insulating properties, h-BN is chemically inert in a wide variety of acids, solvents, and oxidizers. h-BN is insoluble in the usual acids but is soluble in alkaline molten salts and nitrides such as LiOH, KOH, and  $\text{Li}_3\text{BN}_2$ . Owing to its high chemical resistance and thermal stability, h-BN is an attractive material for use as a chemically inert coating in hazardous environments (Liu et al., 2013; Rafiee et al., 2013; Zhi et al., 2009).



## 2. STRUCTURE AND PROPERTIES OF 2D BORON NITRIDE

### 2.1 Structural Properties

The physical form of h-BN is a white slippery powder, analogous to graphite. The flake size of commercially available h-BN ranges from hundreds of nanometers to tens of microns (information obtained from Sigma Aldrich, Alfa Aesar). Hence, the BNNS sheets obtained by exfoliation of these crystals are often limited to the maximum lateral sizes (few tens of microns) of the initial starting material (Bhimanapati et al., 2014). Individual h-BN monolayers or BNNSs are a honeycomb structure with alternating boron and nitrogen atoms. The bond type for B–N is covalent and bond length is 1.45 Å. The distance between the centers of neighboring borazine rings is 2.5 Å. The edge structure for the BNNS can be armchair or zigzag, similar to graphene. The former is a B or N-edged structure, whereas the latter is a BN pair-edged structure. The crystal structure for h-BN is hexagonal with  $\text{P}6_3/\text{mmc}$  space group (Fig. 1A), lattice constants  $a=b=0.2504 \text{ nm}$ ,  $c=0.6661 \text{ nm}$ , bond angles  $\alpha=\beta=90^\circ$ ,  $\gamma=120^\circ$ . The partially ionic structure of BN in h-BN reduces covalency and electrical conductivity and unlike graphite, favors the AA' stacking (Constantinescu et al., 2013). Typically, this is the most energetically favorable stacking observed in BN, where the electron-deficient B atoms are directly above or below the electron-rich N atoms in the adjacent layer (Marom et al., 2010; Warner et al., 2010). The most common way to determine the number of layers in h-BN is by looking at the transmission electron microscopy (TEM) images of the folded edges (Bresnahan et al., 2014; Han et al., 2008; Kim et al., 2012a; Lin et al., 2010a; Pacilé et al., 2008; Shi et al., 2010; Song et al., 2010; Zhi et al., 2009). Fig. 2A and B shows the high-resolution TEM images, which typically gives the number of layers along with more

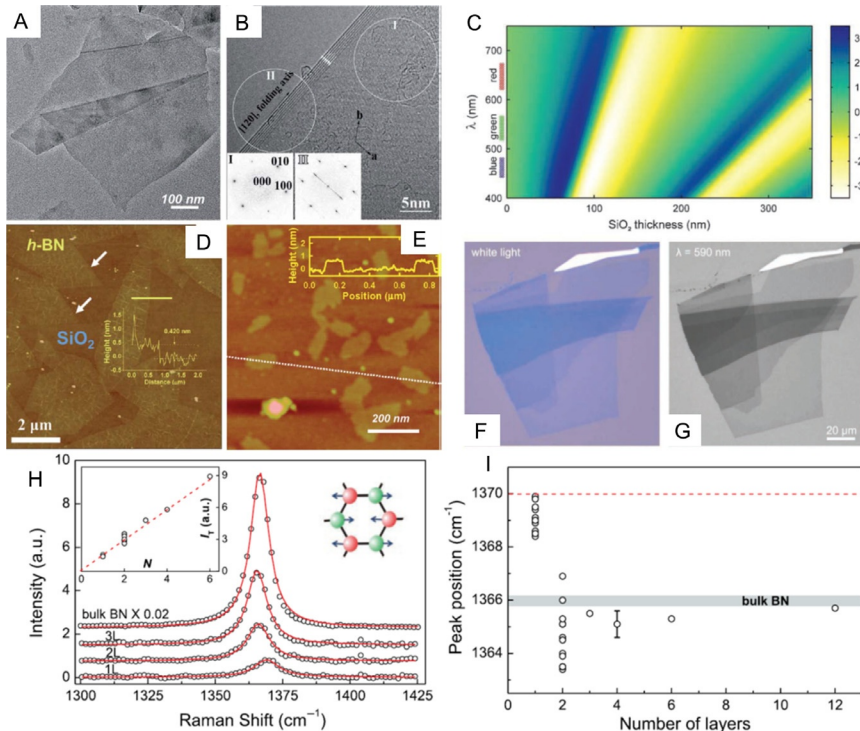


**Fig. 2** (A) Low-magnification TEM image of an exfoliated BNNS. (B) HR-TEM image showing the number of layers at the folded edges ([Lin et al., 2010a](#)). (C and D) AFM height map of CVD grown BNNS showing the monolayer thickness of 0.4 nm. (E) Chemically exfoliated BNNS showing a height of 1 nm. (F) White light microscopy image of exfoliated h-BN flake showing the optical contrast on 90 nm SiO<sub>2</sub>/Si. (G) Improved optical image of h-BN flake using a 590 nm light source showing the different contrast between layers ([Gorbachev et al., 2011](#)). (H) Raman spectra for BNNS to few-layer h-BN comparing the difference in the peak width vs number of layers. (I) Peak position variation as observed for monolayer to bulk BNNS ([Gorbachev et al., 2011](#)).

atomic lattice information. Another simple technique to determine the thickness of h-BN is by using atomic force microscopy (AFM) ([Bhimanapati et al., 2014; Gorbachev et al., 2011; Lin et al., 2010a; Pacilé et al., 2008; Shi et al., 2010; Song et al., 2010](#)). The number of layers can be calculated by looking at the step height typically with respect to the surface ([Fig. 2D and E](#)). Most monolayer h-BN sheets from mechanical exfoliation and chemical vapor deposition (CVD) have a height of ~0.4 nm ([Oliveira et al., 2012](#)). For the chemical exfoliation sheets, the height obtained can vary as much as 1 nm because of the solvent that can

be trapped between the h-BN flakes and the substrate (Lin et al., 2011a). Hence, HRTEM is usually used to report the number of layers and when reporting the height through AFM, more characterization techniques should be used to confirm the findings.

Another simple and convenient technique using an optical microscope was developed to observe the number of layers of graphene sheets and can be employed for h-BN as well (Blake and Hill, 2007). Usually, a standard silicon wafer coated with  $\sim 300$  nm of an SiO<sub>2</sub> layer (Fig. 2C) is used as a reference substrate and the number of layers is predicted based on the optical contrast that was observed using the optical microscope. In the case of h-BN, as it does not absorb in visible region, the substrate oxide layer had to be changed to 80 nm in order to optically identify the mono to few-layered materials. As shown in Fig. 2F, the white light contrast reaches a low of 2.5% for monolayer h-BN, which is four times less than that of graphene, and the contrast increases with the increase in the number of layers (Hod, 2012). Another way to identify the number of layers is by using a different wavelength light, which can be observed in Fig. 2C. By using a light as shown in Fig. 2G with  $\sim 590$  nm wavelength, the contrast between the number of layers was clearly evident.

This layer identification study can further be extended to Raman microscopy (Gorbachev et al., 2011). Boron nitride has a vibrational mode at 1364–1371 cm<sup>-1</sup>, which is dependent on the number of layers. Fig. 2H and I shows the comparative study made by Gorbachev et al. for different layers of BNNS. It can be observed in Fig. 2H that for monolayer, the Raman peak broadens and shifts to a higher wavenumber of 1370 cm<sup>-1</sup> when compared to the bulk, which is at 1366 eV. This study clearly shows the red shift for BNNS formation, which could later be used as a standard to confirm the presence of BNNS.

## 2.2 Thermal Stability

BN allotropes, especially h-BN and the cubic phase of boron nitride (c-BN), exhibit high thermal and chemical stability. h-BN is stable without decomposing at temperatures of over 1000°C in air, 1400°C in vacuum, and up to 2850°C in an inert atmosphere (Paine and Narula, 1990; Sinclair and Simmons, 1987). The theoretical thermal conductivity values for h-BN can be close to graphene ( $\sim 1700$ –2000 W/m K) (Jiang et al., 2009; Lan et al., 2009), one of the best thermally conductive materials available to date (Moore et al., 1992). Depending on the type of BNNS

structure, the zigzag-edged BNNRs are 20% larger than the arm chair-edged nanoribbons at room temperature (Ouyang et al., 2010). In-plane thermal conductivity has been reported as high as 390 W/m K at room temperature, 280 times higher than SiO<sub>2</sub>, making h-BN an attractive dielectric material for heat-generating electronic devices (Ouyang et al., 2010). Similar to graphite, h-BN has a strongly anisotropic coefficient of thermal expansion (CTE) due to its anisotropic bond strength. The CTE in the *a*-direction (in-plane) is  $-2.90 \times 10^{-6} \text{ K}^{-1}$  at room temperature, while the CTE in the *c*-direction is over 10 times larger and  $4.05 \times 10^{-5} \text{ K}^{-1}$  at room temperature (Yates et al., 1975). The large positive thermal expansion in the *c*-direction is due to weak van der Waals bonding between planes.

The most commonly accepted phase diagram of boron nitride was calculated from thermodynamic properties of boron nitride phases by Solozhenko et al. (1999) after refining their original work from 1988. It was found that the c-BN, rather than h-BN, is thermodynamically stable at ambient conditions (Solozhenko et al., 1999). This is in contrast to the carbon phase diagram, where the hexagonal phase (graphite) is the stable phase at ambient conditions (Bundy, 1963). The phase diagram of boron nitride is shown in Fig. 3A and B, where the dashed lines indicate the original calculations by Solozhenko et al. in 1988, and the solid lines indicate the refined diagram. The h-BN/c-BN/liquid triple point occurs at  $3480 \pm 10 \text{ K}$  and  $5.9 \pm 0.1 \text{ GPa}$ , while the h-BN/liquid/vapor triple point occurs at  $3400 \pm 20 \text{ K}$  and  $400 \pm 20 \text{ Pa}$  (Solozhenko et al., 1999).

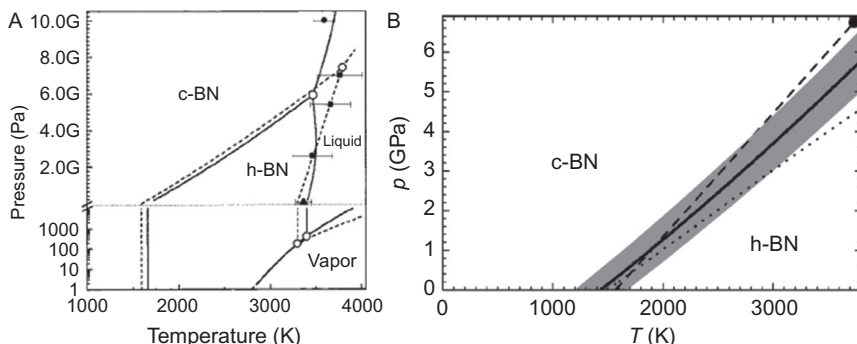


**Fig. 3** (A) Phase diagram of h-BN showing the stability of h-BN vs c-BN at various temperatures and pressures. (B) Close up image of the phase transition and calculations from Solozhenko (dotted line) (Solozhenko et al., 1999).

From the above phase diagram, it is evident that c-BN is more favorable than the h-BN at temperatures below 1600 K. Although this is true, the CVD growth of h-BN, which will be discussed in [Section 3.6](#), was reported on transition metals at much lower temperatures. The typical growth temperatures for CVD are around 700–1100°C, which are at least 300°C cooler than that observed in the general phase diagram. This unusual behavior can be because of the Gibbs free energy of the system. The transition temperature between h-BN and c-BN shifts as a function of Gibbs free energy (Shift  $\pm 10$  meV/atom). This change in the free energy can vary the transition temperature between 1200 and 1800 K, where the lowest value is typically used for the growth of h-BN. These small variations are generally caused by grain size, defects, contaminants, or sometimes interactions with the substrate transition metal itself. Further details about the growth of h-BN is discussed in [Section 3.6](#).



### 3. SYNTHESIS OF BNNS

BNNS can be obtained via top-down (typical exfoliation-type approaches) or bottom-up approaches (usually CVD or other deposition techniques). The most common methods that have been used are mechanical exfoliation ([Chen et al., 2012](#); [Ghosh et al., 2008](#); [Hua Li et al., 2012](#); [Lee et al., 2015](#); [Li et al., 2011a](#)), chemical exfoliation ([Anota et al., 2015](#); [Bhimanapati et al., 2014](#); [Cui et al., 2014](#); [Lee et al., 2015](#); [Li et al., 2013](#); [Lin et al., 2010a](#); [Paton et al., 2014](#); [Roy et al., 2014a](#); [Sainsbury et al., 2012, 2014](#); [Wang et al., 2011a](#); [Warner et al., 2010](#)), CVD ([Bresnahan et al., 2014](#); [Kim et al., 2012a,b, 2013](#); [Lee et al., 2012a,b](#); [Shi et al., 2010](#); [Song et al., 2010](#)), and pulsed laser deposition (PLD) ([Glavin et al., 2014](#)). Most of these methods have their own advantages and disadvantages, as they are used for specific targeted applications. BNNS isolated from exfoliation techniques are usually crystalline, although obtaining a high percentage of exfoliated sheets is very difficult. Using these exfoliation techniques, obtaining a higher density of monolayer flakes is really difficult and time consuming. Also, because of the strong lip–lip interactions between the layers, there is high probability of layer stacking on top of each other. In contrast, CVD techniques use the breakdown of precursors and results in a highly controllable process of making BNNS. Typically, the crystallinity obtained via CVD is less than that when compared with exfoliation techniques.

### 3.1 Mechanical Exfoliation

Mechanical exfoliation, also known as the “scotch tape method,” or micro-mechanical cleavage method, uses scotch tape as a very simple tool for exfoliation (Novoselov et al., 2004). Using this technique, isolation of layers can be controlled down to a monolayer and the flake size depends on the biggest flake available for exfoliation. The final BNNS obtained via this technique retains the original lateral size and low defect density as the parent h-BN crystal used. As a variety of nanosheets can be easily obtained with this technique, fundamental studies in physics and electronics have been done mostly using the materials obtained via exfoliation (Alem et al., 2009; Gorbachev et al., 2011; Jin et al., 2009; Meyer et al., 2009; Novoselov et al., 2005; Pacilé et al., 2008). Compared to other exfoliation methods, the mechanical exfoliation method is the least scalable technique, especially for large-scale applications. Other reports using mechanical cleavage methods beyond simple mechanical exfoliation have been explored to produce large quantities of BNNS. As these materials are bonded by weak van der Waals forces, techniques with shear forces like a ball mill technique were used (Hua Li et al., 2012; Li et al., 2011a). Traditional ball mill techniques are very aggressive, nonselective, and yielded significant number of defects in the exfoliated material (Ghosh et al., 2008; Lee et al., 2015; Li et al., 2011b; Lin et al., 2010b). Although this technique yields a better output than mechanical exfoliation, the defect density in the final exfoliated films is higher. Further improvements to the ball milling technique were also used by using a solvent along with the ball milling process (Fig. 4A). Li et al. reported that using a mild wet ball milling process (Li et al., 2011b), few-layered crystalline BNNS with only a slight

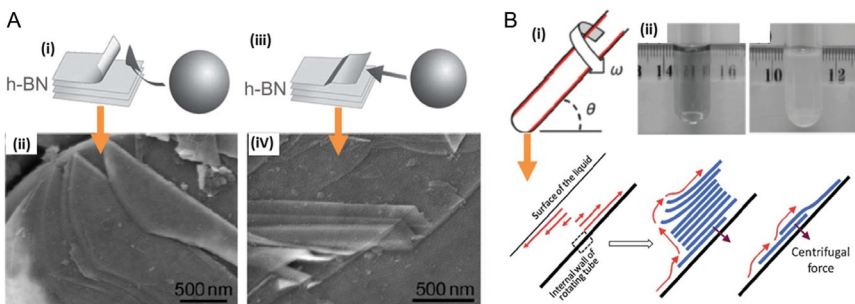


**Fig. 4** (A) (i and iii) Wet ball mill process used for the mechanical exfoliation process (Li et al., 2011b), (ii and iv) SEM images showing the exfoliation process mechanism. (B) (i) Mechanism of vortex fluidic process (Chen et al., 2012) which was operated at 8000 rpm. This process works on centrifugal force for exfoliation, which can be observed in the figure and (ii) image showing the uniform dispersion before and after the process.

lateral size reduction was obtained. Various solvents have been tested in wet ball milling. Benzyl benzoate was an effective lubricant because of its weight, which provided better exfoliation results than water, ethanol, or dodecane (Deepika et al., 2014). As selection of the solvent is important for exfoliation, which can be obtained by looking at the weight of the solvent and the surface tension properties of the solvent and h-BN. Further, use of planetary mill instead of the more aggressive high-energy mills provide uniform rolling motions of the balls applying predominantly shear force to the h-BN flakes (Hua Li et al., 2012; Yao et al., 2012). Further, use of smaller diameter balls instead of the heavier balls added additional lubrication for the interaction, which reduced the loss of the BNNS sheet size.

Another setup that was used for this type of exfoliation is the vortex fluidic device (Chen et al., 2012). As it can be observed in Fig. 4B, a small amount of h-BN suspension in *N*-methyl-2-pyrrolidone (NMP) was rotated at 8000 rpm in a glass tube with a fixed angle of the fork which resulted in significant exfoliation of the h-BN crystals. The presence of NMP formed a thin layer on the inner walls of the centrifuge tube and the rotating shaft, which at an angle, provides enough shear force to partially exfoliate the layers in the liquid mixture. Further, a more scalable approach was proposed based on this technique (Fig. 5A). Here, a high-pressure microfluidization process (Yurdakul et al., 2012) was used in a continuous

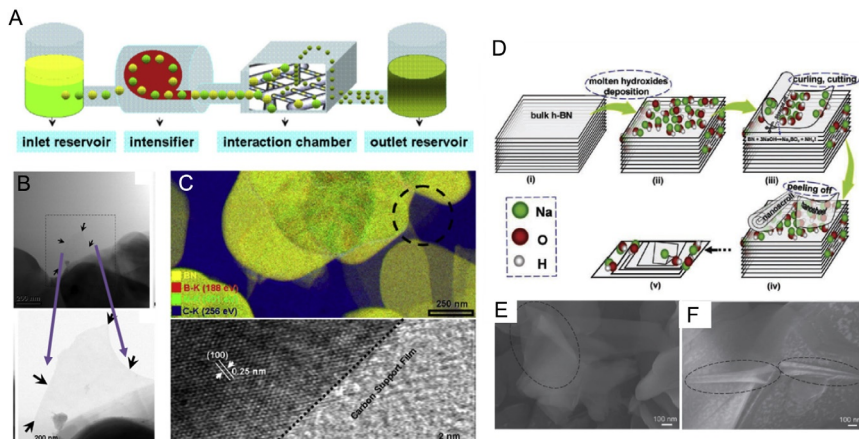


**Fig. 5** (A) Flow diagram showing the microfluidization process (Yurdakul et al., 2012) used for exfoliation. (B) TEM image showing the presence of ultrathin BNNS achieved from this process. (C) Elemental mapping and lattice spacing obtained in high-resolution TEM confirming the presence of h-BN. (D) Mechanism of dry exfoliation process using molten hydroxides (Li et al., 2013) ( $\text{NaOH}$ ,  $\text{KOH}$ ). (E and F) SEM images showing the curling of h-BN sheets and formation of nanoscrolls of h-BN.

flow setup by using h-BN flakes and a polar organic solvent which was pumped through a microfluidic processor at a high pressure of 207 MPa, circulated continuously for multiple times. At these high pressures, the liquid generates a large shear force, which results in exfoliation of h-BN particles with a reported yield efficiency of 45%. High-resolution TEM mapping clearly showed that the final exfoliated material was h-BN without any functional groups and defects.

Dry mechanical process can also be used for the exfoliation process (Li et al., 2013), which is achieved by using molten hydroxides. The most common chemicals used in this case are sodium hydroxide (NaOH) and potassium hydroxide (KOH). This process involves that the hydroxide and the h-BN powder was ground together then transferred into a polytetrafluoroethylene-lined stainless steel autoclave where the reaction takes place at 180°C for 2 h. This process is used for making nanoscrolls of BNNS. The exfoliation process follows a sequence of steps that are shown in Fig. 5D. The first step involves the self-curling of the h-BN sheets at the edges after the molten hydroxide is attached on the surface layer. Subsequently, the anions and the cations enter the interlayer space and the adsorbed anion ( $\text{OH}^-$ ) radicals start curling process in the adsorbed layer and finally, the peeling away of the parent material is observed as a result of this curling process. As this process is easy and involves low-cost method, it can be scalable. The final product obtained can be transferred to any solvents or to any substrates.

### 3.2 Solvent-Assisted Ultrasonication

Sonication-assisted exfoliation has been a common approach and has been used widely across various 2D material systems. The general idea in this process is to disperse the boron nitride in a solvent and with the aid of sonication power, the sample tends to exfoliate because of the energy that is generated by the sonication process. Surfactants can also be added to improve the dispersion of the nanoparticles.

In order to understand the dispersion ability for 2D materials, Coleman et al. (2011) and Shen et al. (2015) attempted to understand the direct solvent dispersion of 2D materials by using Hansen solubility parameter theory. They postulated that in order to select a good solvent or a mixture of solvents for direct dispersion enthalpy of mixing must be minimized, and hence the energy of the exfoliation is minimized. This means that the solvent should possess a similar surface energy as that of the nanosheets (Fig. 6A). In the case

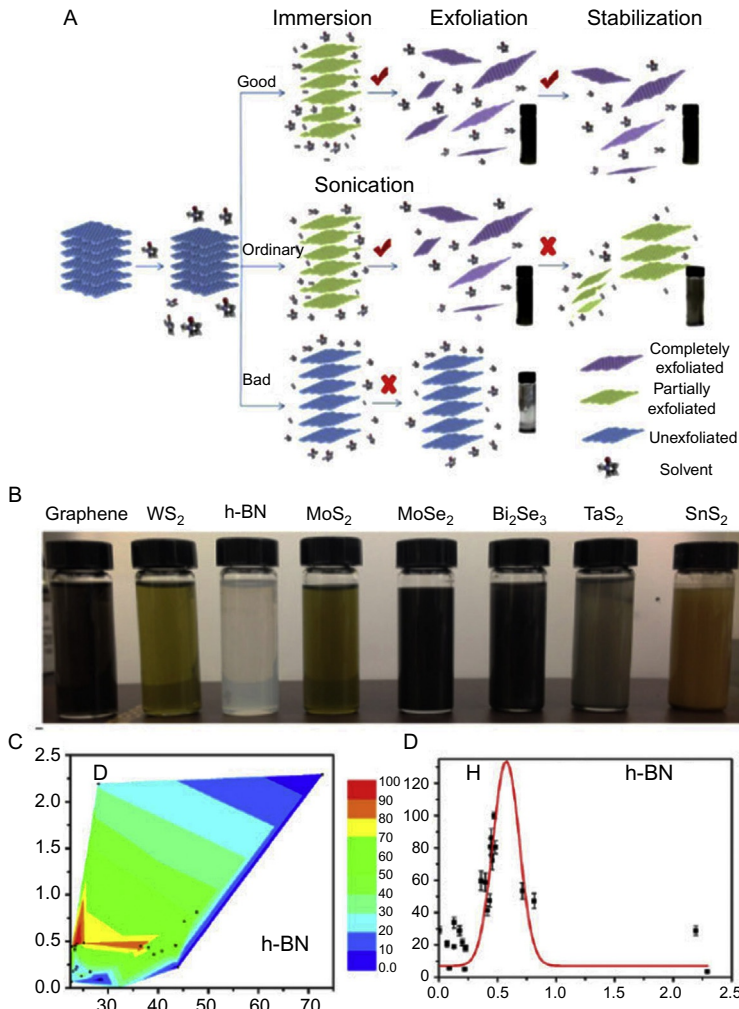


**Fig. 6** (A) Proposed mechanism for liquid-phase exfoliation by matching the solvent surface tension with the 2D material ([Shen et al., 2015](#)). (B) Image showing the dispersion of various solvents. (C and D) Dispersion of h-BN as a function of total surface tension and polar dispersive ratio (panel D is fitted with a Lorentzian peak function).

of boron nitride, a surface energy of around  $65 \text{ mJ/m}^2$  was proposed to be ideal and because of this, BNNS usually were formed in solvents such as iso-propylalcohol (IPA) or NMP. This theory is true for most of the 2D materials ([Fig. 6B](#)) where the surface energy  $\sim 70 \text{ mJ/m}^2$  or a surface tension of  $\sim 40 \text{ mJ/m}^2$  would provide the best possible results ([Coleman et al., 2011](#)). The dispersion ratio for h-BN with varying concentrations is listed in

**Fig. 6C and D.** Certain mixture of solvents based on ethanol and water were also used which showed improved exfoliation and dispersion than when used individually.

Although this model holds for most solvents, certain solvents tend to deviate from this behavior because they tend to interact with the nanomaterials much more strongly and can even chemically react with the material. One good example is water. Although water does not wet h-BN at room temperature and was proposed to be hydrophobic, it was found to be counter intuitive when reports claimed to show high dispersion of BNNS in water (Li et al., 2013; Lin et al., 2011a). Also, it was shown that BNNS dispersion contains a very high fraction of exfoliated sheets (~20%) than that of the other solvents. This unusual behavior can be accounted to the reactivity of h-BN, which could yield boron oxide and ammonia when it was treated in hydrolysis conditions. The mechanism of exfoliation can be observed in Fig. 7A. Hence, after the exfoliation process, a small amount of

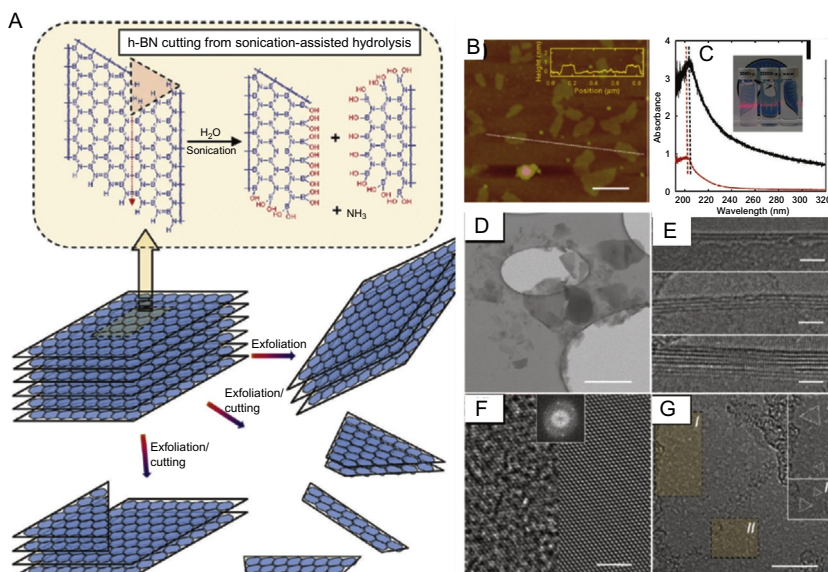


**Fig. 7** (A) Image showing the sonicated assisted hydrolysis of h-BN to form BNNS (Lin et al., 2011a). Using a high polar solvent, exfoliation and cutting of the nanosheets are possible. (B) Image showing the BNNS flakes obtained after the exfoliation process with a thickness of 1 nm. (C) Optical absorption of BNNS suspended in solvents. (D and E) TEM images showing the BNNS flakes obtained and by looking at the edges, different thickness BNNS are obtained. (F and G) HRTEM image showing the monolayer BNNS structure and the defects in the material.

boron oxide and dissolved ammonia was found in the solvent and OH functionality was present on the surface of the h-BN. This presence of OH functionality on the surface further yielded the additional stability and dispersibility in water (Fig. 7B–G).

### 3.3 Acid Exfoliation

Boron nitride is typically neutral when reacting to acids. General acids do not show a high degree of exfoliation, although using a high protic acid such as (Wang et al., 2011b), methyl sulfonic acid (MSA) exfoliation was much more successful. Concentrations of up to 0.3 mg/mL were obtained when bulk BN was dispersed and sonicated in MSA, which was comparable to water or other solvents. Similar to the graphite exfoliation by hummer's process, BNNSs are also protonated at the edges and surface during this process, which lead to repulsive forces between the layers. This was further supported by looking at the color change that occurred after the reaction. The BNNS dispersed in MSA turned orange which could be because of the charge transfer between acid molecules and nanosheets. This color was later changed to milky white when redispersed back into other organic solvents. Further characterization using FTIR and X-ray photoelectron spectroscopy (XPS) showed that there was no presence of additional bonding which indicated that the BNNS was not functionalized (Wang et al., 2011b). Another approach using modified hummer's process was made by Bhimanapati et al. (2014) for exfoliation of h-BN. Hummer's process did not affect the boron nitride although, tampering the temperature and time of reaction in the hummers process provided enough time for the permanganate ions and the acid solution to intercalate between the h-BN sheets thereby forming BNNS. The BNNS could be later dispersed in various solvents still retaining the functional groups.

### 3.4 Chemical Functionalization of h-BN

Utilizing chemical functionalization for exfoliation has proved effective for the case of graphite allotropes, especially CNTs (Cui et al., 2010; Kuila et al., 2012). Similar strategies have been used in the case of BN to achieve exfoliation via functionalization of the surface. Typically, BN is resistant to wet and dry oxidation, although 2D and 1D BN are ionically active to functionalization due to the local polarization of B–N bonding. A simple way to functionalize BNNS includes heating h-BN in air to a high temperature (~800°C) (Cui et al., 2014). Heating h-BN in air leads to the incorporation

of small amounts of oxygen into the lattice of the h-BN (Cui et al., 2014), which is followed by stirring in DI water to incorporate a B–O functionality. The stirring mechanism leads to the formation of the functional groups that result in separation of the h-BN layers into BNNSs. As this process involves heating and dispersion in water, it could be termed as a similar approach to sonication in DI water process. The yield obtained through this process is small (~2–4%). In order to completely functionalize the BNNS, the functionalization approaches can be divided into three major categories: noncovalent type functionalization, ionic functionalization or Lewis acid–base functionalization, and covalent functionalization.

### 3.4.1 Noncovalent Functionalization

Noncovalent functionalization is typically obtained by using a polymer or a copolymer. These polymers typically tend to functionalize via the  $\pi$ – $\pi$  interactions between the polymer and the h-BN sheets. The polarity of the functional molecule plays a major role in its optimal orientation on the h-BN sheets (Gao et al., 2014; Grimme, 2011; Grimme et al., 2007). The lowest energy molecular interactions will be governed by the electrostatic interactions between the functional polymer and the boron nitride sheets. Several polymers such as poly(*m*-phenylenevinylene), 2,5-dioctoxy-*p*-phenylenevinylene, tetracyanoquinodimethane, and tetraphiafulvalene were used to study the functionalization mechanism. Recently, BNNS were noncovalently functionalized using polyvinyl alcohol (PVA) and later attached to a paper with natural nacre (Zeng et al., 2015) (Fig. 8A). This noncovalent functionalized approach drastically improved the mechanical and thermal performance of the natural nacre, which were also proposed to be used as substrates for electronics. Also, several transition metal arene complexes were also predicted to noncovalently functionalize h-BN. It was predicted from theory that the stable configuration for the transition metal arenes to functionalize is by having a metal atom at the center of the borazine rings. Most of the time after functionalization, band gap reduction and spin polarization are observed in h-BN, indicating the success of functionalization. Further ab initio studies showed that h-BN can also be attached with DNA and RNA molecules (Ding et al., 2013; Lin et al., 2011b) (Fig. 8B), where the N and O atoms of the nucleobases are located above the B atoms. Further, the nucleobases prefer to attach facially rather than perpendicularly because the noncovalent interaction is higher than the  $\pi$ – $\pi$  interactions. This could lead to a better biomedical applications using h-BN.

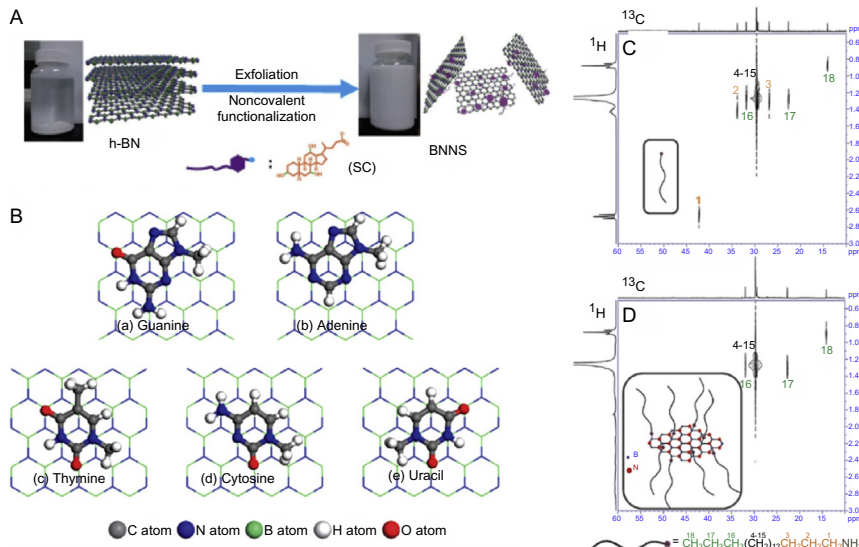


**Fig. 8** (A) Noncovalent functionalization of BNNS using polyvinyl alcohol (PVA) which improves the dispersion of the BNNS in solvents, used in thermal and mechanical composites (Zeng et al., 2015). (B) Ab initio calculations for optimized structure configurations for different nucleobases adsorbed on BNNS for bioapplications (Lin et al., 2011b). (C) Amine functional group addition on the BNNS and NMR spectra confirming the presence of ODA-BN functionalization (Lin et al., 2010a). (D) Dibromomocarbene (DBC) addition on BNNS via aqueous heating in sodium hydroxide (Sainsbury et al., 2014).

### 3.4.2 Ionic Functionalization (or Lewis Acid–Base Interactions)

The boron atom in the h-BN lattice is electron deficient and possesses Lewis acid characteristics, making it susceptible to attack by a Lewis base molecule such as amines or phosphines to form stable Lewis acid–base complexes. Although there are reports on the boron atom being ionically functionalized (Lin et al., 2010a; Xie et al., 2005; Yu et al., 2012), there was no experimental reports on nitrogen atom although it is electrophilic in nature. Because of the B–N bonding being locally polarized, in theory it should be a convenient target for both the atoms to get ionically functionalized.

Several attempts have been made to demonstrate the Lewis acid–base interactions on h-BN using amino groups of octadecylamine (ODA), amine-terminated oligomeric polyethylene glycol, trioctylamine, and tri-octylphosphine (Lin et al., 2010a,b). The lipophilic and hydrophilic chains of these molecules intercalated into the h-BN layers and functionalized the sheets which were later extracted by dispersing in water or organic solvents. The final dispersed material was still transparent for lower concentrations and milky white for higher concentrations. Lateral sizes of ~1 µm and

thickness of about 1–7 nm were obtained via this process. Trace amounts of monolayer materials were also obtained, but the lateral sizes were <100 nm. To further improve the efficiency of functionalization, defects were created on h-BN sheets by ball milling the h-BN powder (Lin et al., 2010b). These defects were confirmed by X-ray diffraction and Raman as the (002) peak and the in-plane mode ( $E_{2g}$  peak) broaden when defects are introduced. After defects were introduced, there was better solubility after the functionalization. This was further confirmed using NMR spectroscopy which is observed in Fig. 8C and D (Lin et al., 2010a; Yu et al., 2012). The alkyl radicals on the amino-terminated region were observed for its C–H signals, which were reduced from the parent material, indicating that this end was attached to the h-BN. Further studies on the defect h-BN starting material showed a shifting position of the same C–H signals of the ODA functional group. This indicated that the amino end of the ODA molecule that was attached to the B atoms and the boron sites contained the defects.

### 3.4.3 Covalent Functionalization

Direct covalent functionalization is not possible, as BN is very chemically stable material. Several functional groups have been added covalently onto h-BN sheets and typically adhere to the edges and basal planes of the material. In order to attach the functionalization and exfoliation via covalent functionalization, several treatments have to be made. Recent reports showed that Hummer's process with modifications in the temperature worked effectively for creating oxygen bonding on the boron sites. The confirmation of the bonding was observed through XPS and FTIR where B–O bond was present. Other approaches were also made by attaching hydroxyl groups, a nitrene (methylphenylcarbonate) via a thermal oxidation and treatment with strong oxidants. These were mostly used in the applications for polymer composites which improved the performance of the composite. For specific targeted applications, silver nanoparticles were further decorated after hydroxyl functionalization on the BN sheets (Fig. 9A and B) (Roy et al., 2014a). Coleman et al. also functionalized BNNS using dibromocarbene (DBC). In their work, they used BNNS as a 2D phase transfer catalyst for the carbene migration across the organic–aqueous phase boundary. The BNNS formed B–CBr<sub>2</sub> bonding in order to stabilize the carbenes which also act as the reactive substrate for the functionalization. The functionalization reaction is shown in Fig. 9D. This functionalization resulted in the formation of B–C and B–N bonds on the BNNS lattice by forming dibromo-bridged bicyclic BCN linkage. This covalent chemistry

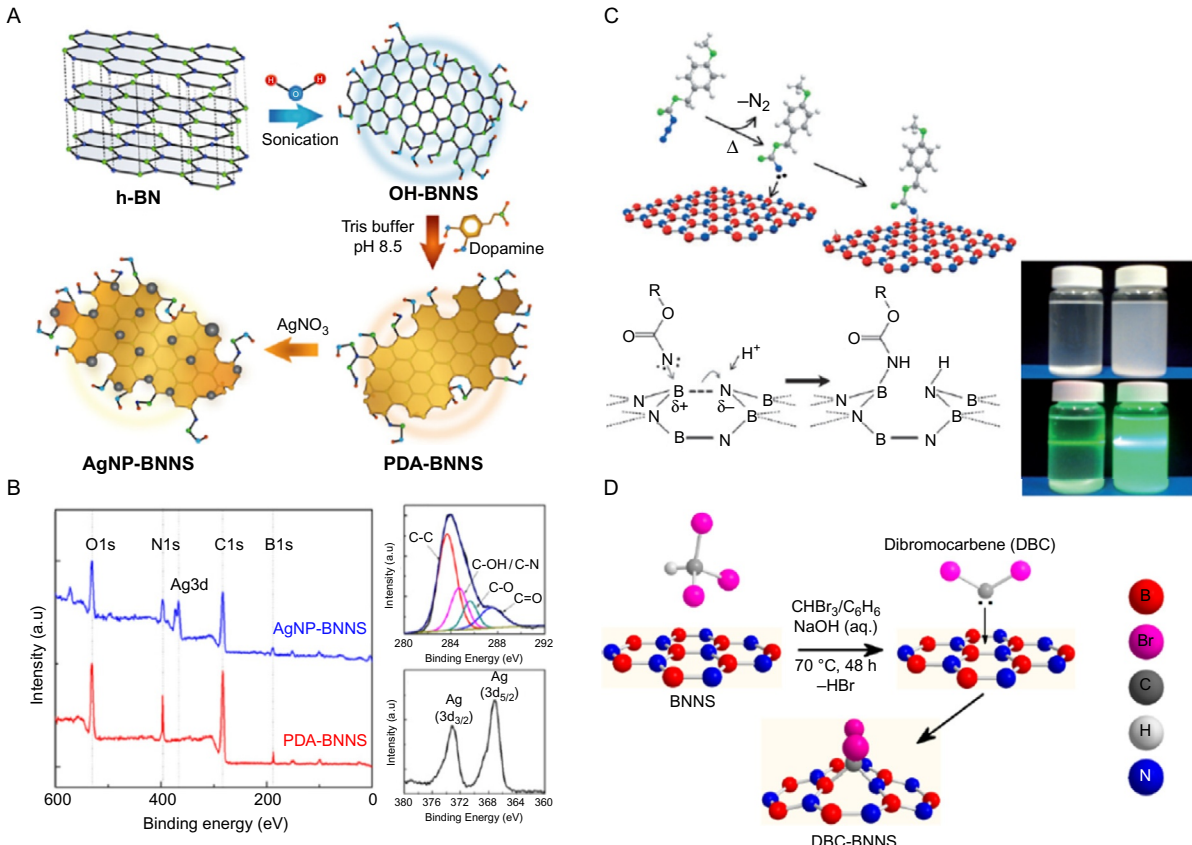


**Fig. 9** Covalent functionalization of h-BN nanosheets using different functional groups. (A) Hydroxyl functionalization of the BNNS sheets and later decorating it with silver nanoparticles ([Roy et al., 2014a](#)). (B) XPS spectra confirming the presence of the functionalization and the decoration of Ag on BNNS. (C) Nitrene addition on BNNS, covalently bonded on to the phase and edge sites ([Sainsbury et al., 2012](#)) (inset image showing the dispersion and absorption change in the BNNS before and after functionalization). (D) Dibromocarbene (DBC) addition on BNNS via aqueous heating in sodium hydroxide ([Sainsbury et al., 2014](#)).

was confirmed using multiple different characterization techniques. This CBr<sub>2</sub> linkage on the BNNS was later used to interface with solvents, which can later be integrated in polymer composites easily (Sainsbury et al., 2014). Further, similar work was extended to functionalize the BNNS by nitrene addition (Sainsbury et al., 2012). 4-Methoxybenzyloxycarbonylazide was used as the source to functionalize it. This type of functionalization mostly attacks the B atoms in the h-BN lattice, resulting in breaking of B–N bonds in the structure. This reaction changes the milky white color of BNNS to dark brown generating N<sub>2</sub> bubbles and creating reactive nitrene radicals. This later yields the formation of methoxylphenyl carbamate bound to BNNS via the B–N bond as shown in Fig. 9C. Most of the functionalization approaches result in highly dispersed BNNS in solvents which can later be integrated into many different applications. Typically, most of these processes were used to make polymer composites to improve thermal and mechanical strength of the polymers.

### 3.5 Unzipping of BNNTs

Another method to synthesize h-BN sheets is by unzipping BNNTs. Various approaches have been utilized to unzip BNNTs. The process of obtaining BNNS through unzipping of BNNTs is typically used to study the properties of the edges that are obtained through this process. One interesting property to note is that BNNS obtained from BNNTs are only ~15 nm wide and semiconducting because of the small dimensions.

The first reported approach described first dispersing the BNNTs in polymers, followed by etching the polymer away (Zeng et al., 2010). In this case, the BNNTs need to be well dispersed in solution and dried on a substrate—typically Si or SiO<sub>2</sub>. This unzipping process can be observed in Fig. 10A. A polymer solution (PMMA) is then spin coated on the silicon substrate until the polymer matrix is formed on the surface. It is subsequently peeled off from the substrate leaving a BNNT encapsulated polymer film. Finally, the BNNT is subjected to etching via an inert gas or plasma treatment. The etching process takes place until a part of the BNNT is cut leaving us with layers of BNNS (Fig. 10A). This process can be treated as a controllable way to synthesize h-BN nanosheets as most of the samples are protected by the polymer matrix and only a selected few area is etched away. The etched BNNTs are then dispersed in solvents and sonicated to obtain individual sheets of h-BN. Further confirmation of the unzipping process was observed using TEM (Fig. 10B and C).

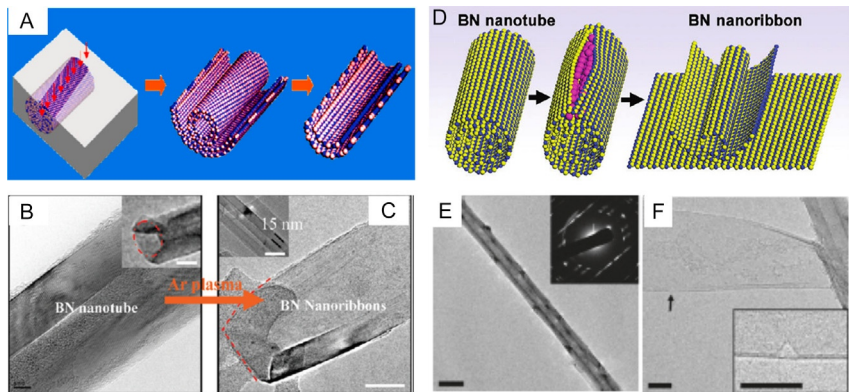


**Fig. 10** (A) Unfolding mechanism of BNNTs encapsulated in a polymer matrix (Zeng et al., 2010). (B) TEM image showing the BNNT before exfoliation and (C) TEM showing the BNRR obtained after the controlled plasma etching of BNNTs. (D) Alkali salt intercalation mechanism of BNNT where the alkali salt is attached on the lateral side of the BNNT and the exfoliation along the longitudinal side (Erickson et al., 2011). (E and F) TEM images showing the exfoliation of BNNT to BNRR after the alkali intercalation and washing the salt in water.

Another approach to unzipping BNNTs is by using an alkali metal intercalant (Erickson et al., 2011), as shown in Fig. 10D. This process is more difficult than that of graphite, as h-BN is less vulnerable to intercalants. Erickson et al. (2011) vaporized potassium metal into the walls of the nanotubes for intercalation as shown in Fig. 10E. This process was performed at 300°C for almost 72 h in vacuum and is efficient for inducing longitudinal splitting of BNNTs. Although this process used an external deposition of metal to break the sheets, sheets over 1-μm long with widths up to 50 nm were obtained (Fig. 10F). The interplanar spacing for BNNS intercalated with potassium was found to be 5.8 Å (Okada and Otani, 2010). This significant increase in the wall spacing for BNNT (from ~3.33 Å) will result in circumferential strain on the bonds. This strain later breaks the bonds at the weakest points, resulting in exfoliation. This technique suffers from low yield (~1%) and this is a not a bulk process. The intercalated potassium atoms will form islands on the surface which continuously grew inducing circumferential strain around the nanotube surface which led to bond breakage at the weakest points. As this is a slow process, most of the etched nanosheets were still attached to the parent nanotubes, which were then removed later by sonication in solvents such as IPA. Using this process, the nanoribbons obtained will inherit the same structural properties as that of the parent nanotubes (Kosynkin et al., 2011). This process could

potentially be scalable approach to make nanoribbons of h-BN by looking into the cleaning process after the reaction.

### 3.6 Single and Few-Layer h-BN via CVD

Nucleation and growth methodologies for high-quality mono- and few-layer h-BN films, as well as many other 2D material counterparts, have been of significant interest within the past decade. The necessity for direct growth, in contrast to the previously discussed exfoliation techniques, is driven by the desire for large area film coverage with strict control of layered thickness as well as eliminating the difficulties associated with the lift-off and transfer processes seen in many exfoliation variations (Bresnahan et al., 2013; Geim and Grigorieva, 2013). To date, the progress in growth of 2D insulators including h-BN has significantly lagged behind comparable conductors and semiconductors (eg, graphene, transition metal dichalcogenides, and other 2D material systems), as the difficulty in materials processing presents many challenges for device usage (Osada and Sasaki, 2012). These difficulties include lack of large area growth required for electronic devices, compatibilities with substrate materials, and required high-deposition temperatures (typically  $>1000^{\circ}\text{C}$ ), each that will be discussed in following sections.

Even as the overall interest in 2D materials has increased substantially since the isolation and initial studies at the University of Manchester (Novoselov et al., 2004), monolayer and few-layer h-BN has been directly grown in small domains since the mid-1990s. One of these first isolations of monolayer h-BN was made possible by Nagashima (Nagashima et al., 1996; Rokuta et al., 1997) and was performed by thermal decomposition of borazene ( $\text{B}_3\text{N}_3\text{H}_6$ ) at  $700\text{--}800^{\circ}\text{C}$  on metallic substrates including nickel ( $\text{Ni}(111)$ ), palladium ( $\text{Pd}(111)$ ), and platinum ( $\text{Pt}(111)$ ), which continue to be common substrates for h-BN growth. Initial studies using EELS and XPS led to key observations including the realization of very low interaction energy between h-BN and the substrate, as well as the extremely slow growth rate for the second layer of h-BN from a lack of reactivity on the surface of the monolayer islands. These studies were performed with limited interest at the time, but would later influence the 2D materials community substantially nearly a decade later.

Once the exciting discovery of graphene ignited the research in the topic of 2D materials in the mid-2000s, CVD became the most prominent growth technique used for single and few-layer 2D materials, including h-BN. Demonstration of large area growth of few-layer h-BN by atmospheric

pressure CVD (APCVD) in early 2010 yielded highly uniform films on copper foil with thicknesses of a few atomic layers (Shi et al., 2010; Song et al., 2010). The precursor reactants in these initial studies included ammonia borane ( $\text{NH}_3\text{-BH}_3$ ), a solid powder requiring sublimation at temperatures of 120–130°C, as well as a gaseous precursor borazene, also used in initial studies by Nagashima (Nagashima et al., 1996). Both studies were performed at substrate temperatures of 600–700°C for 20–30 min of growth in an Ar/H<sub>2</sub> gas mixture, followed by a postannealing step at 1000°C to further crystallize the multilayer film. The similarities in film growth and structure for initial efforts in CVD h-BN coatings are represented in Fig. 11, where Fig. 11A–C shows an optical image of the few-layer h-BN film, high-resolution “top-down” TEM view of the atomic structure, and cross-sectional TEM image of the few-layer h-BN film, respectively, from

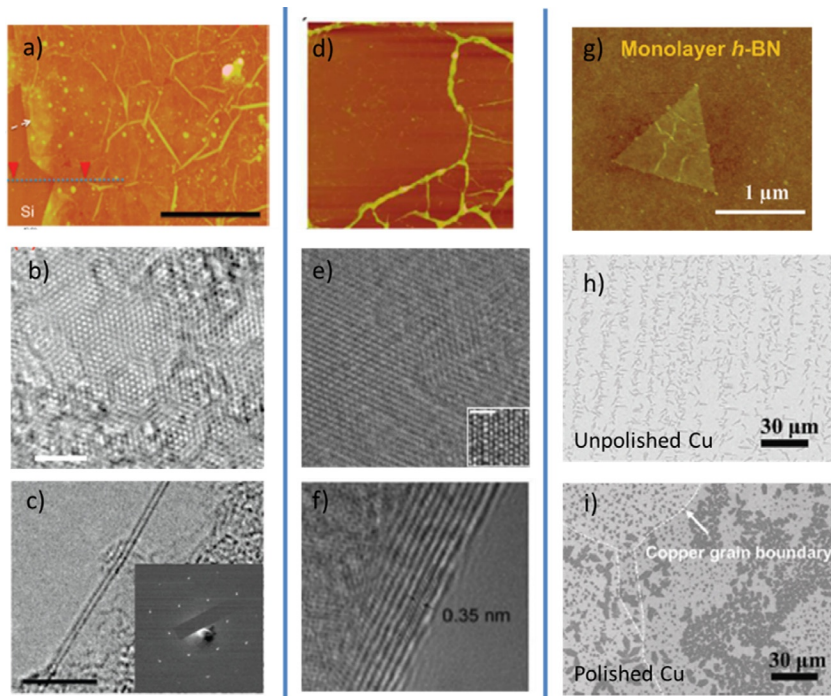


**Fig. 11** (A) An optical top-down view of the as-deposited h-BN on Silicon, (B) a close-up TEM micrograph of the hexagonal patterning in h-BN, and (C) a cross-sectional view of few-layer h-BN growth (Song et al., 2010). Similar images from Shi et al. (2010) in (D)–(F). The last column in Fig. 1 is from Kim et al. (2012a) with (G) an SEM image of monolayer triangle formation of h-BN, (H) optical image of h-BN growth on unpolished, and (I) highly polished copper foil.

Song et al. (2010). Fig. 11D–F displays complementary images using the same techniques from Shi et al. (2010). The first growth procedures for the ultrathin h-BN coatings identified many critical issues, common in current growth methods as well, including the necessity to reduce wrinkles, cranks, and pinholes, as the need for uniform, large area coverage is required for many applications.

It was not until 2012, when Kim et al. (2012a) were able to isolate repeatable, triangular domains of single layer h-BN by performing the growth at lower pressures (technique known as LPCVD) using borazene, a gaseous species slightly more environmentally stable than borazene when decomposed. Advantages of the LPCVD synthesis include increased cleanliness in a vacuum environment, reduced activation energy for h-BN formation at lower pressures (Vlassiouk et al., 2013), as well as the reduced effect of kinetics and dynamics of the inlet gas flow for growth (Bhaviripudi et al., 2010). Fig. 1E is an optical image of one of the triangular domains, with grain sizes on the order of 1 μm. At a single layer, the reactivity of the h-BN is very low and can lead to incomplete film coverage in this instance of monolayer triangles. Additionally, the surface conditions of the substrate play a critical role in the nucleation density as well as the growth dynamics (Lee et al., 2012b), evidenced by the optical images of the distribution of domains of h-BN seen in Fig. 11H and I of the same growth conditions on unpolished and polished copper foil, respectively (Kim et al., 2012a).

At the time, it was a surprise that the first domains of h-BN were triangular, in contrast to the traditional hexagonal pattern seen in graphene synthesis on copper foil (Cu) (Tang et al., 2013a). Origins of these triangle domains are attributed to low reactivity of the nitrogen-terminated edges (Fig. 12A) (Liu et al., 2011) that restrict the lateral growth of the triangular domains. As graphene is a monatomic structure, the lack of contrasting edge site nucleation forms a hexagonal pattern similar to the internal structure of the graphene rings. It was observed by Stehle et al. (2015) that by altering the location of the substrate in the tube (ie, further or closer to reactant source), and thus altering the nitrogen-to-boron active species concentrations in the gas phase at the substrate location, the shape of these few micron-sized domains can be altered from triangle to semi-hexagons, as seen in Fig. 12B. Further manipulation of gas flow dynamics in the CVD tube (more substantial impact at atmospheric pressure growth) has also proven to control the nucleation shape of the h-BN domains from controllable triangles to more advanced structures (Yin et al., 2015).

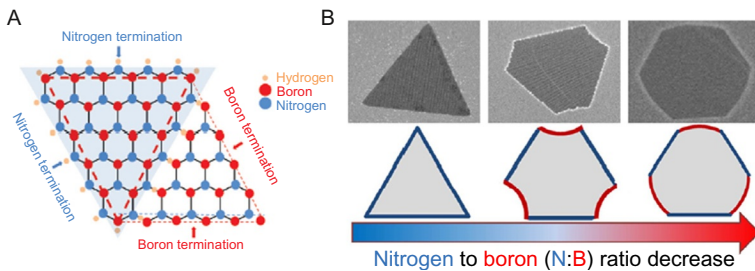


**Fig. 12** (A) Representative schematic of the triangle formation of h-BN, where the nitrogen termination is the more energetically favorable termination and (B) the change in h-BN initial grain formation shape as a function of nitrogen and boron chemical concentrations in the CVD furnace. Panel (A) from Kim, K.K., Hsu, A., Jia, X., Kim, S.M., Shi, Y., Hofmann, M., et al., 2012. Synthesis of monolayer hexagonal boron nitride on Cu foil using chemical vapor deposition. *Nano Lett.* 12, 161–6. doi:10.1021/nl203249a. Panel (B) from Stehle, Y., Meyer, H.M., Unocic, R.R., Kidder, M., Polizos, G., Datskos, P.G., et al., 2015. Synthesis of hexagonal boron nitride monolayer: control of nucleation and crystal morphology. *Chem. Mater.* 27, 8041–8047. doi:10.1021/acs.chemmater.5b03607, acs.chemmater.5b03607.

Beyond h-BN growth on copper foils, 2D h-BN nucleation and growth have continued to expand to other metals including various crystal orientations of Ni (Cho et al., 2015; Preobrajenski et al., 2005; Yang et al., 2015; Zhang et al., 2014), Pt (Kim et al., 2013), Pd (Morscher et al., 2006), and alloys of these materials (Lu et al., 2015). Nickel, in particular the (111) crystal orientation, has shown to facilitate high-quality h-BN growth due to the small lattice mismatch (0.4%). This strain induced by the difference in lattice mismatch is compensated by a slight corrugation of the ad layer, and the periodicity of this depends on the degree of lattice mismatch between the substrates (Morscher et al., 2006). Grain size of the 2D h-BN can be directly influenced by the surface structure, as exemplified by record high triangular grain size of  $7500 \mu\text{m}^2$  on Cu/Al alloys at growth temperatures of  $1050^\circ\text{C}$  (Lu et al., 2015). The authors attribute the large grain size to the small addition of Al in the alloy, where the nucleation density can be decreased to 60 sites per  $\text{mm}^2$ , leading to unimpeded, large crystal growth on the surface.

Other interesting 2D structures can be formed by epitaxial lattice interactions between the substrate and h-BN. h-BN nanomesh, a porous material consisting of 12 substrate unit cells with aperture structures 2 nm in width, can be formed on ruthenium (Ru(0001)) and rhodium (Rh(111)) by LPCVD techniques used for monolayer growth on other foils (Corso et al., 2004; Goriachko et al., 2007). These structures form upon the decomposition of borazine vapor at temperatures at  $1100^\circ\text{C}$  and can have a

particular benefit for use in patterning and assembly of nanoparticles such as gold nanoclusters. The change in nanostructure simply by altering the surface lattice structure and texturing conditions highlights the fact that h-BN in both the monolayer and few-layer form is extremely surface sensitive during the nucleation and growth process.

The majority of CVD synthesis routes have been focused on metallic substrates, as the foils can withstand high-temperature synthesis (800–1000°C) and can have epitaxial-like growth effects. Ideally, the 2D material can be grown directly on substrates of greater interest for electronics and other applications. If this would be possible, the requirement for the time and personnel-intensive lift-off and transfer steps would be eliminated, streamlining the device construction process. Prospects for direct growth of h-BN on alumina ( $\text{Al}_2\text{O}_3$ ) and silica ( $\text{SiO}_2$ ), both common substrates for nanoelectronic applications, are discussed by [Bresnahan et al. \(2013, 2014\)](#). Key aspects of the h-BN growth such as stoichiometry as a function of growth temperature, crystal size, and thermal transport properties were evaluated to elucidate how the thin h-BN films would behave in a graphene device construct. In addition, the enhancement of graphene hole concentration and mobility was evaluated with respect to the quality of the as-deposited films on  $\text{Al}_2\text{O}_3$  and  $\text{SiO}_2$ . Direct growth of the turbostatic, 2D h-BN films processed at 400°C was shown to possess a higher boron content, however, show the largest increase in mobility of the graphene layered on top of the film, with a 1.5 × and 2.5 × increase compared to  $\text{Al}_2\text{O}_3$  and  $\text{SiO}_2$ , respectively.

In parallel to the initial studies involving CVD nucleation and growth, physical vapor deposition techniques have also become of great interest for growth of few-layer h-BN. Physical vapor deposition techniques including PLD, magnetron sputtering, and molecular beam epitaxy (MBE) have all proven to facilitate h-BN growth at various conditions. In these cases, the use of a high-energy plasma (in the case of PLD and sputtering) or molecular beam is initiated in an ultrahigh vacuum chamber (typically residual base pressures of  $10^{-7}$ – $10^{-8}$  Pa). The plasma or molecular beam then comes in contact with the substrate and condenses to form thin films of h-BN.

With the use of high-energy plasmas, several benefits over conventional CVD approaches including reduced required temperature for h-BN formation, large area coverage, and versatility in device fabrication. The plasma-based techniques including magnetron sputtering as well as PLD have been used to coat very large wafers with uniform, cohesive thin films on the order

of 4" in diameter and larger. Due to the high-energy plasma species, however, special considerations need to be addressed as to how to control the kinetically driven processes to resist damage to the substrate and reduce the nucleation site density to allow for large area, unimpeded grain formation. [Sutter et al. \(2013\)](#) using reactive magnetron sputtering from a boron source in an Ar/N<sub>2</sub> gas mixture (see [Fig. 13A](#)) was able to generate a very slow flux of energetic ions and neutral species to the surface to condense and form uniform, highly crystalline multilayer h-BN on a Ru substrate, seen in [Fig. 13B](#). With a three-step process combination of initial CVD to seed the growth to less than a monolayer, following by sputtering at high and low temperatures for subsequent multilayer growth, multiple layers can be formed with a varying degree of thicknesses and stoichiometry, as measured by XPS in [Fig. 13C](#) and D. [Glavin et al. \(2014\)](#) described that in PLD from an amorphous boron nitride target, a highly stoichiometric B–N plasma can be formed, and a recipe can be constructed where the stoichiometry of the as-deposited BN film can be uniform regardless of substrate. By appropriately choosing the working distance from target to substrate and adjusting the background pressure to facilitate shock-wave-like plasma dynamics, the appropriate precursors for stoichiometric h-BN formation can be realized, regardless of surface conditions. The structure, however, is very dependent upon the surface, as a highly dense amorphous boron nitride film is formed on most substrates, and a nanocrystalline h-BN is grown on nearly lattice-matched substrates including HOPG at temperatures of 700°C. The growth procedure is fairly quick, at ~0.4 nm/laser pulse, where the laser pulses are at 1 Hz repetition rate. Because of the high deposition rate, the nucleation density is also very high, resulting in grain size formation of 3 nm. The film, however, is cohesive and uniform over the substrates of interest, yielded similar electronic tunneling properties at all measured locations on the substrate. Other PLD studies using very high-energy CO<sub>2</sub> lasers have shown to produce high-quality h-BN nanosheets that overlap and form on the substrate surface at an even lower temperature of 400°C ([Sajjad et al., 2013](#)).

Studies of MBE of h-BN growth on nickel foils by [Nakhaie et al. \(2015\)](#) were able to use energy from the molecular ion beam, namely an elemental B and N source, to form large area, cohesive thin films of h-BN. The mixture of the high-energy molecular flux, coupled with the high surface temperatures, can lead to interesting metastable structures that are not necessarily bound to triangular film formation seen in CVD. [Fig. 13A](#) and a close-up in [Fig. 13B](#) provide images of MBE growth of h-BN that can result in

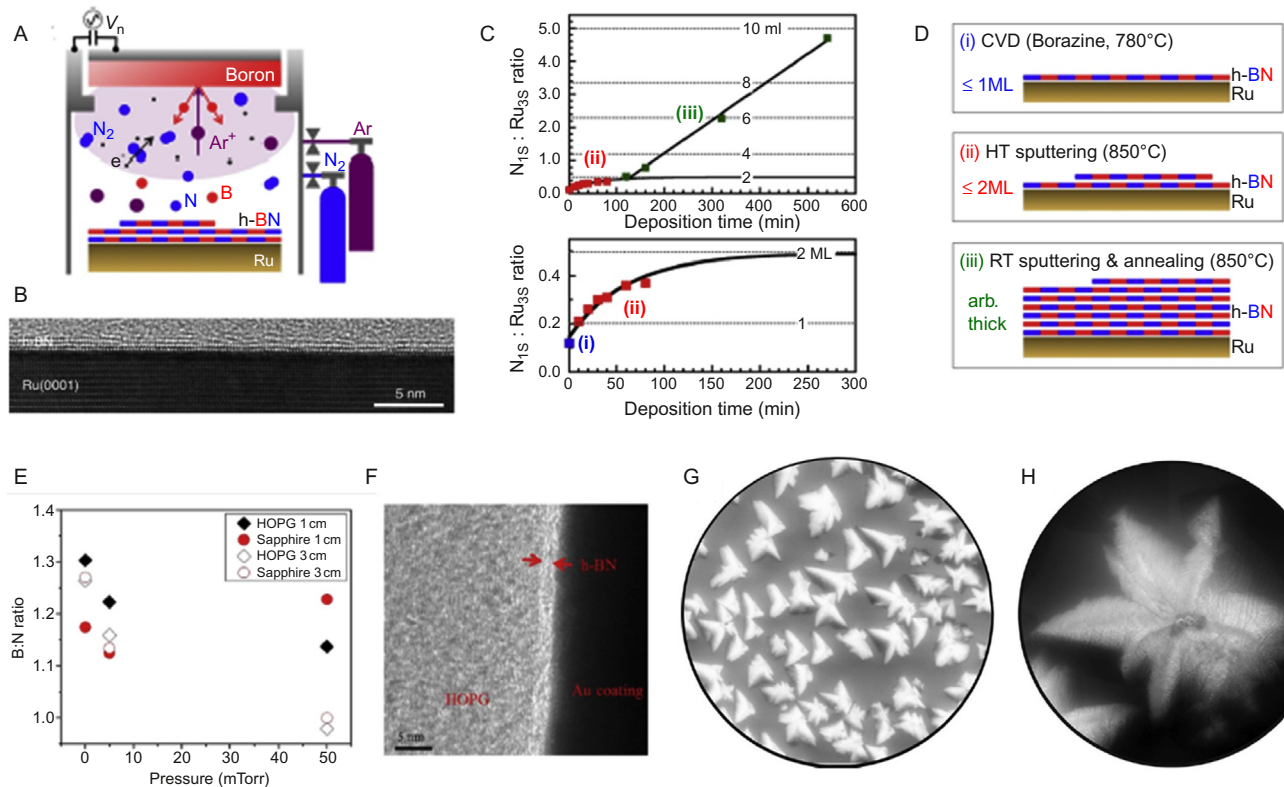


**Fig. 13** (A) Setup of reactive magnetron sputtering for h-BN films, (B) cross-sectional TEM image of few-layer growth on Ru (0001), (C) XPS analysis of thickness for the different growth conditions, and (D) outlining the three-step process for arbitrarily thick h-BN coatings. The next two images portray h-BN growth with PLD processing of (E) the B:N ratio measured by XPS as a function of background gas nitrogen pressure and working distance in the chamber and (F) a cross-sectional image of few-layer h-BN on HOPG. The two final images are of MBE of h-BN with (G) initial h-BN grain formation and (H) a close-up of a similar image, window sizes of 30 and 9 μm, respectively. *Panels (A–D) from Sutter, P., Lahiri, J., Zahl, P., Wang, B., Sutter, E., 2013. Scalable synthesis of uniform few-layer hexagonal boron nitride dielectric films. Nano Lett. 13, 276–281. doi:10.1021/nl304080y. Panel (H) from Nakhaie S., Wofford J.M., Schumann T., Jahn U., Ramsteiner M., Hanke M., et al., 2015. Synthesis of atomically thin hexagonal boron nitride films on nickel foils by molecular beam epitaxy. Appl. Phys. Lett. 106, 213108. doi:10.1063/1.4921921.*

flower-like configurations, which eventually nucleate and grow in ways that are not traditional in CVD reactor chambers. These can be attributed to the additional kinetic energy (Barth et al., 2005) supplied by the incoming beam, where the addition of this energy can lead to a reduction in required growth temperature, evidence by growth of these initial flower-like growths at 730°C.

2D h-BN is one of the more interesting 2D materials to date, and direct growth methods to understand how to enhance and control the film formation are critical to the future of nanoelectronic devices, anticorrosive coatings, and other uses. Advances in CVD processing have resulted in extremely large grain size, stoichiometric films, and alternative processes including PLD and plasma-based processing techniques could allow for realization of direct-growth device constructs.

### 3.7 Defect Manipulation in h-BN Using Scanning Tunneling Microscopy

h-BN is insulating, hence characterization of defects using scanning tunneling microscopy (STM) requires the use of a graphene capping layer because of the lack of conduction drain path for the electrical current (Wong et al., 2015). In order to observe the different defects in boron nitride, a graphene/boron nitride heterostructure was made. This allowed the visualization of the defect phenomenon in the underlying boron nitride.

Electronic configuration of the BN defects from the STM  $dI/dV$  signal was measured and quantified from the graphene capping layer. For the ring defects, the gate ( $V_g$ ) and the bias ( $V_b$ ) voltages were analyzed which were dependent on the ring radius. This was attributed to the charging of the adsorbate or the defect. Depending on the response time when the STM tip was present, the defect can be narrowed to the top most layer which is strongly coupled with the graphene electronic structure. Further, the defect manipulation was performed using STM. Fig. 14A shows the presence of numerous charged defects in the h-BN sheet. In order to manipulate the defects, the STM tip was placed 1 nm over the center of the defect area and a bias voltage was applied. After the voltage pulse, the  $dI/dV$  map was acquired again for the same region at low bias as observed in Fig. 14B. From Fig. 14B and C, it can be observed that the defect configuration was significantly altered by applying voltage pulses. The defects would switch reversibly between charged state and neutral state by applying the voltage across the sheet. These defects also switched between states having opposite charges. This can be observed in Fig. 14B and C with the red, blue, and green arrows. This tip-induced manipulation can be explained by electric field

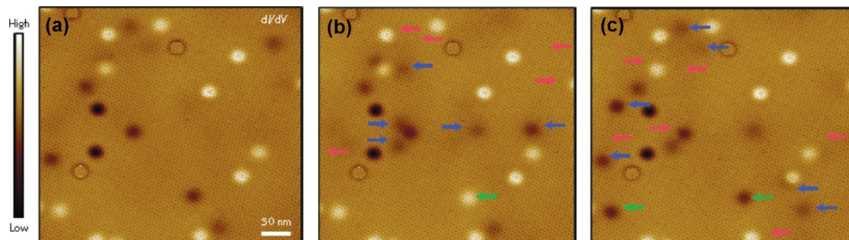


**Fig. 14** Defect manipulation in h-BN using an STM tip. A tip pulse of  $V_s = 5$  V and  $t = 10$  s was used to alter the charge states of the defects. (A)  $dI/dV$  map of graphene/h-BN reveals various dot and ring defects in the h-BN sheet, (B)  $dI/dV$  map of the same region after one-tip pulse applied at the center, and (C)  $dI/dV$  map of the same region after two-tip pulses on the h-BN. The red (gray in the print version) arrow corresponds to the disappearance of the dot defects relative to previous image, blue (dark gray in the print version) arrow shows the appearance of the same defects, and the green (light gray in the print version) arrow shows the dot defects that have changed sign of their charge (Wong et al., 2015).

induction emission of the charge carriers from the defect states of h-BN. The STM tip causes charge carriers to tunnel through the ionization barrier between different defects, which allows partial charging and partial neutralization of the other points. This would explain the appearance and disappearance of the dot defects, which are not as a part of defect migration in BN lattice. Hence, this allowed the imaging and manipulation of individual defects in the insulating BN substrate with the help of a graphene capping layer.

## 4. APPLICATIONS FOR 2D h-BN ATOMIC LAYERS

Two-dimensional h-BN has been considered for use in many different applications including gate and substrate dielectrics for nanoelectronic devices, anticorrosive coatings, frictional layered coatings, high-temperature resistive layers, and other advanced applications for 2D material systems. The large bandgap ( $\sim 6$  eV), high temperature and chemical resistivity, and other properties discussed earlier in the chapter make both the exfoliated h-BN and direct-grown h-BN material ideal for such applications.

### 4.1 Dielectrics in Next-Generation Nanoelectronic Devices

Graphene is known for having one of the highest electron and hole mobility of any material to date, making the 2D material a natural candidate for next generation high-speed electronic devices (Bolotin et al., 2008). Initial

graphene devices transferred onto traditional  $\text{SiO}_2$  substrates were observed to have a reduction in intrinsic transport properties due to adverse interactions with the substrate ( $>120,000 \text{ cm}^2/\text{Vs}$  compared to device performance on  $\text{SiO}_2$  of  $\sim 2000 \text{ cm}^2/\text{Vs}$ ) (Liao et al., 2010; Lin et al., 2010c). The carrier mobility in the devices was reduced due to the scattering from charged surface states and impurities in  $\text{SiO}_2$ , the relatively high surface roughness of the substrate, and the low-frequency surface optical phonon modes in  $\text{SiO}_2$  (Chen et al., 2008b; Martin et al., 2008; Morozov et al., 2008). Dean et al. (2010) was the first to investigate the use of bulk h-BN as a substrate material to counteract these effects seen in  $\text{SiO}_2$  devices. The strong in-plane bonding of the h-BN substrate was hypothesized to allow for an atomically smooth, inert surface free of dangling bonds, or surface charge traps. This was found to be true, as the electronic properties of graphene including enhanced mobility, reduction in carrier inhomogeneity, and reduced intrinsic doping from the substrate were substantially improved. Wang et al. (2011c) demonstrated the first exfoliated GFET with h-BN integrated in both the substrate and gate dielectric, effectively creating a h-BN/graphene/h-BN sandwiched device. When compared to a traditional GFET device with  $\text{SiO}_2$  and  $\text{Al}_2\text{O}_3$  as dielectrics, an increase of 70% in the peak transconductance ( $g_m$ ) was observed with a higher frequency of operation, as well as a greater than  $5 \times$  increase in graphene mobility from 1200 to  $6500 \text{ cm}^2/\text{Vs}$ . Additionally, Dean et al. (2012) demonstrated a similar device construct using exfoliated materials, where the flakes can be seen in Fig. 15A and a hall device setup in Fig. 15B for electron mobility measurements. The devices display a mean electron mobility of  $\sim 35,000 \text{ cm}^2/\text{Vs}$ , with measurements as high as  $\sim 70,000 \text{ cm}^2/\text{Vs}$ . These mobility values are of a substantial increase of nearly an order of magnitude higher than similar graphene devices on  $\text{SiO}_2$ . Also, the charge neutrality point of the graphene is shifted to near zero gate voltage, as seen in Fig. 15C on a series of devices. This increase in mobility is also observed in polycrystalline CVD graphene on h-BN, where an increase of greater than three times is observed in Fig. 15D (Gannett et al., 2011), an effect seen in other device constructs as well (Nayfeh et al., 2013).

h-BN is also of interest as a key component as a gate dielectric in graphene and other 2D material-based electronic devices. With a dielectric constant of 6, breakdown voltage of 8–10 MV/cm, and bandgap nearing 6 eV (Lee et al., 2011; Watanabe et al., 2004), advantageous over conventional  $\text{SiO}_2$  dielectrics can be realized. In the first demonstration of a 2D material component device, exfoliated h-BN was the choice of gate

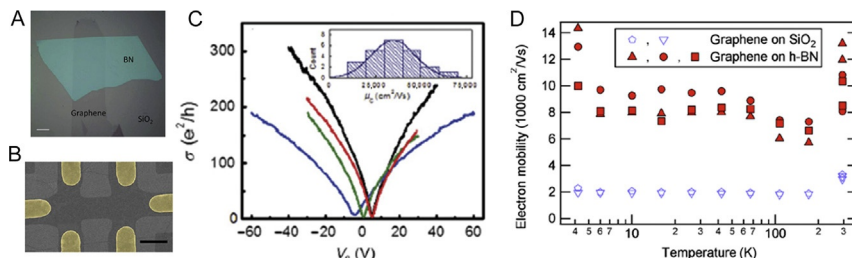


**Fig. 15** (A) Optical image of graphene and h-BN flakes (scale bar 10  $\mu\text{m}$ ), (B) optical image of a hall bar measurements device for graphene electron mobility (scale bar 1  $\mu\text{m}$ ), (C) electron mobility as a function of gate voltage, with a histogram of mobility seen in inset, and (D) electron mobility enhancement in graphene on h-BN at various temperature as compared to graphene on SiO<sub>2</sub>. Panels (A–C) Dean, C., Young, A.F., Wang, L., Meric, I., Lee, G.H., Watanabe, K., et al., 2012. Graphene based heterostructures. Solid State Commun. 152, 1275–1282. doi:10.1016/j.ssc.2012.04.021. Panel (D) from Gannett, W., Regan, W., Watanabe, K., Taniguchi, T., Crommie, M.F., Zettl, A., 2011. Boron nitride substrates for high mobility chemical vapor deposited graphene. Appl. Phys. Lett. 98, 242105. doi:10.1063/1.3599708.

dielectric with MoS<sub>2</sub> as the working material and graphene as the electrical contacts, providing for a unique device architecture based on all van der Waals solids (Roy et al., 2014b). The thickness of h-BN in this instance was very thick in this case, around 55 nm. While this device exemplifies rectifying behavior with high-quality interfaces between the materials, all of the 2D components were carefully exfoliated and placed in their given location. Thus, the meticulous device construction does not elude to further scale-up required for real world applications. Ideally, devices in the future can incorporate a directly grown synthesis method, such as CVD growth of h-BN, described earlier in this chapter. In addition, the prospect toward flexible, transparent devices has also been explored (Lee et al., 2013). Kim et al. (2012b) describe device-scale dielectric properties of the CVD grown h-BN, where at 15–19 nm, the film measures a dielectric constant of 2–4 with a breakdown of  $2.0 \pm 0.5$  MV/cm. The decrease in breakdown and dielectric constant is attributed to the polycrystallinity of the h-BN films, potentially allowing for leakage through the grain boundaries. In order to incorporate h-BN as a gate dielectric material in next generation 2D devices, it appears that leakage through these boundaries will be critical with regard to dielectric and device performance.

## 4.2 Vertical Tunneling Device and Behavior

In addition to BN as a substrate material for graphene electronics, few-layer boron nitride has been investigated as a high-quality, low-dielectric constant barrier material for the 2D vertical electron tunneling devices where electrodes of different compositions are separated by the layer thickness of the dielectric. These devices rely on the tunneling through the ultrathin crystalline films layers and allow for the smallest allowable gate lengths down to a single atom, allowing for extremely fast transport ([Tang et al., 2013b](#)).

Tunneling measurements through few-layer, exfoliated h-BN for device constructs have been performed on a conductive substrate using conductive atomic force microscopy (C-AFM). With effective tip areas typically on the order of  $10^3 \text{ nm}^2$ , intrinsic property values of the dielectric can be evaluated that are not dependent on typical macro- or microscopic dielectric failure mechanisms including dust particles, cross-plane defects, and grain edges. From these measurements,  $I-V$  curves were generated on pristine crystalline BN flakes of various thicknesses from [Lee et al. \(2011\)](#). At mono-, bi-, and trilayer h-BN films, direct tunneling was observed as the dominant transport mechanism, seen in [Fig. 16A](#). Beyond this thickness, the resulting  $I-V$  curves obeyed a more traditional breakdown behavior. This study indicates that four atomic layers of h-BN is the required thickness to restrict direct tunneling behavior in 2D h-BN. Similar studies were performed using a top and bottom graphene electrode setup, seen in [Fig. 16C](#) from [Britnell et al. \(2012\)](#). Using a C-AFM setup, as depicted in [Fig. 16D](#), can help identify the tunneling through the BN flake on a device-scale contact setup. With this technique, the thickness and corresponding resistance values can be mapped out as portrayed in [Fig. 16E](#) and F.

[Fig. 16B](#) clearly shows that there are two regimes associated with tunneling in ultrathin h-BN materials of thicknesses greater than three layers (not direct tunneling). At low biases, the  $I-V$  curves will start out linear and then eventually become exponentially dependent at higher biases (typically  $>0.5 \text{ V}$  for monolayer h-BN). At the lower voltages, the tunneling barrier has not been significantly deformed by the applied electric field. Thus, the tunneling current is linearly dependent upon the applied voltage and exponentially dependent upon the thickness of the layered material, as expected for direct tunneling ([Bumm et al., 1999](#)). The tunneling current at this regime can be modeled using the following relationship:

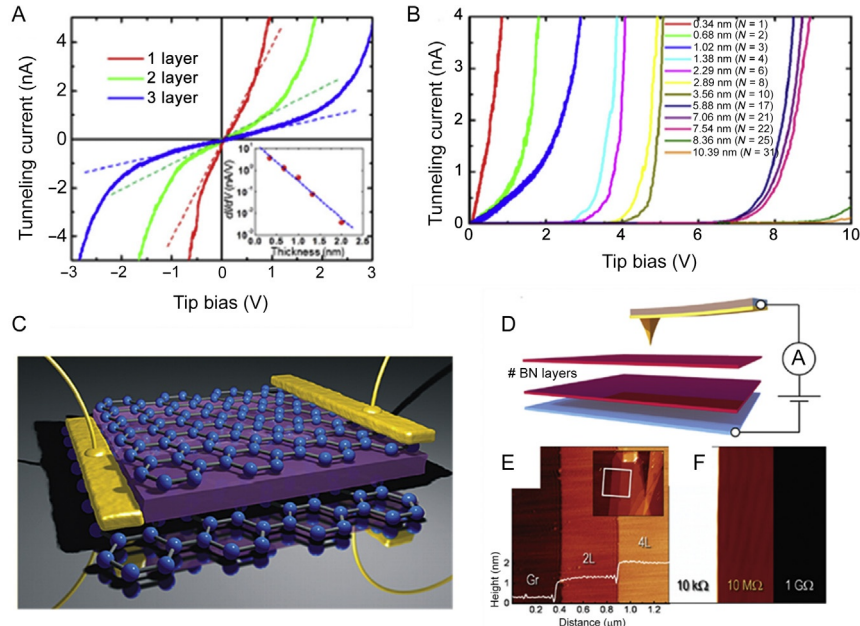


**Fig. 16** (A)  $I$ – $V$  curves generated from C-AFM studies on mono-, bi-, and trilayer films, as well as (B) thicker films up to 31 layers. In addition, device studies from [Britnell et al. \(2012\)](#) using a setup described in (C) and (D), and resulting electrical resistivity behavior in multiple layers of h-BN in (E) and (F). *Panel (A) from Lee, G.-H., Yu, Y.-J., Lee, C., Dean, C., Shepard, K.L., Kim, P., et al., 2011. Electron tunneling through atomically flat and ultrathin hexagonal boron nitride. Appl. Phys. Lett. 99, 243114. doi:10.1063/1.3662043.*

$$I(V) = \frac{A_{\text{eff}} \sqrt{m\phi_B} q^2 V}{h^2 d} * \exp \left[ \frac{-4\pi \sqrt{m\phi_B} d}{h} \right]$$

where  $q$ ,  $m$ ,  $d$ , and  $h$  are the charge of an electron, free electron mass, film thickness, and Plank's constant, respectively. The effective area of contact  $A_{\text{eff}}$  is typically the area of the contacted tip, and  $\phi_B$  is the barrier height. Direct tunneling was only able to be completely resolved at thicknesses typically less than about 2 nm, as direct tunneling is not measurable in thicker films because of the low probability of electrons tunneling through the barrier.

At higher applied biases, the tunneling is dominated by field-emission tunneling across the barrier, and the voltage dependence becomes quadratic. In this regime, modeling using the Fowler–Nordheim tunneling ([Britnell et al., 2012](#)) theory is performed with the following  $I$ – $V$  equation:

$$I(V) = \frac{A_{\text{eff}} q^3 m V^2}{8\pi h \phi_B d^2 m^*} * \exp \left[ \frac{-8\pi \sqrt{2m^*} \phi_B^{2/3} d}{3hqV} \right],$$

where effective mass ( $m^*/m$ ) is 0.26 for h-BN. The voltage is high enough at this point to alter the barrier characteristics and a significant reduction in resistivity is observed, leading to a breakdown in the dielectric characteristics within the material.

Determination of the barrier height is critical in understanding electronic behavior of a semiconductor or insulator and the interface of a metal. Depending upon the barrier height and the interface qualities, the Fermi level can potentially be pinned, resulting in rectifying characteristics within the Schottky barrier. Using the above equations, the barrier height can be determined if the affective contact area is known. [Lee et al. \(2011\)](#) measured the barrier height to be  $3.07 \pm 0.3$  eV in h-BN, which is very close to that of traditional  $\text{SiO}_2$  dielectric (3.25 eV). Another critical piece of information that can be obtained from the C-AFM experiments on tunneling through crystalline materials is the dielectric breakdown strength. In [Fig. 16B](#), the breakdown strength is shown to be linearly dependent upon film thickness up to relatively thick films. Using the constant current method ([Boucart and Ionescu, 2008](#)), pristine h-BN exfoliated flakes appear to have measured dielectric breakdown strength of 8–10 MV/cm ([Britnell et al., 2012; Lee et al., 2011](#)), which, like to the barrier height, happens to be a very similar value to that of comparable  $\text{SiO}_2$ .

### 4.3 h-BN in Protective Coatings

While research on h-BN has focused on nanoelectronic applications, other technologies utilizing the ultrathin, layered materials have also been impactful. Thin h-BN for corrosion and antioxidation coatings, in particular, is a technology that is enabled by the chemical inertness and high temperature stability of h-BN ([Jacobson et al., 1999](#)), to effectively seal the underlying material from exposure to a variety of elements ([Liu et al., 2013](#)). Initial studies indicate that grown of few-layer h-BN on Ni can withstand oxidation up to temperatures as high as 1100°C, even in oxygen-rich atmospheres, as displayed in [Fig. 17](#), with an SEM before (A) and after (B) image ([Liu et al., 2013](#)). In addition, the weight gain as a function of temperature and several different coating thicknesses can be resolved in [Fig. 17C](#). The coating technique can also be used for other 2D materials, as graphene was shown in the same study to withstand oxidation up to temperatures of 1000°C. The main

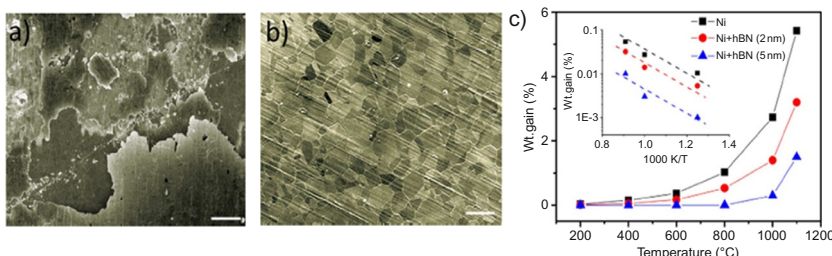
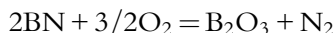


**Fig. 17** (A) SEM images of nickel oxidation at 1100°C without h-BN coating and (B) with h-BN coating (no oxidation), and (C) weight gain percentage at various temperature, showing the change in oxygenation at these conditions (Liu et al., 2013).

reaction associated with BN and oxygen involves the decomposition of the BN itself into boric acid under the following reaction (Jacobson et al., 1999):



The large activation energy required to break this BN molecule ( $\sim 13$  eV) lends itself to the explanation as a great antioxidaion coating, where other oxidation reactions of the underlying substrates can be much lower energies of formation (Liu et al., 2013).

The antioxidative properties, as well as the ultrathin nature of 2D h-BN, can also be utilized in sensing platforms to effectively seal the active material from the element, but not impede in the sensing capabilities. Take for instance, the study performed by Liu et al. (2015) where an MoS<sub>2</sub> transistor setup was used to measure various gases including acetonitrile, ethanol, methanol, and various other gases. When the exfoliated h-BN cap protecting the MoS<sub>2</sub>, the sensing ability was not degraded, and the lifetime of the device was extended to 7 days when capped, compared to 1 day uncapped.

Due to the inert nature and lack of dangling bonds, as discussed earlier, h-BN can be an excellent antifriction coating, similar to many other 2D materials that share the same characteristics (Lee et al., 2010). When reducing friction, a monolayer of coverage may actually be detrimental, and a thickness of at least a few layers may be required to reduce the frictional characteristics. The mechanism describing this phenomenon involves the fact that single layers tend to induce “puckering,” where the AFM tip creates out of plane deformation of the 2D material. This effect is mitigated as the thicknesses increases, and the stiffness of the resulting layers restricts this. Still, flakes of h-BN and other materials pose to have a great impact in antifrictional coatings in the near future.

#### 4.4 h-BN in Gas Sensing

More recently, h-BN has been used as a substrate to detect gases such as ammonia and ethanol (Liu et al., 2015; Postole et al., 2005; Xu et al., 2013). Gas sensors were made using atomic layers of h-BN and a very low concentration (100 ppm) of gases was passed through the device (Lin et al., 2016). The mechanism of the detection is shown in Fig. 18A, where the conductance change is measured which is caused by the chemical absorption and

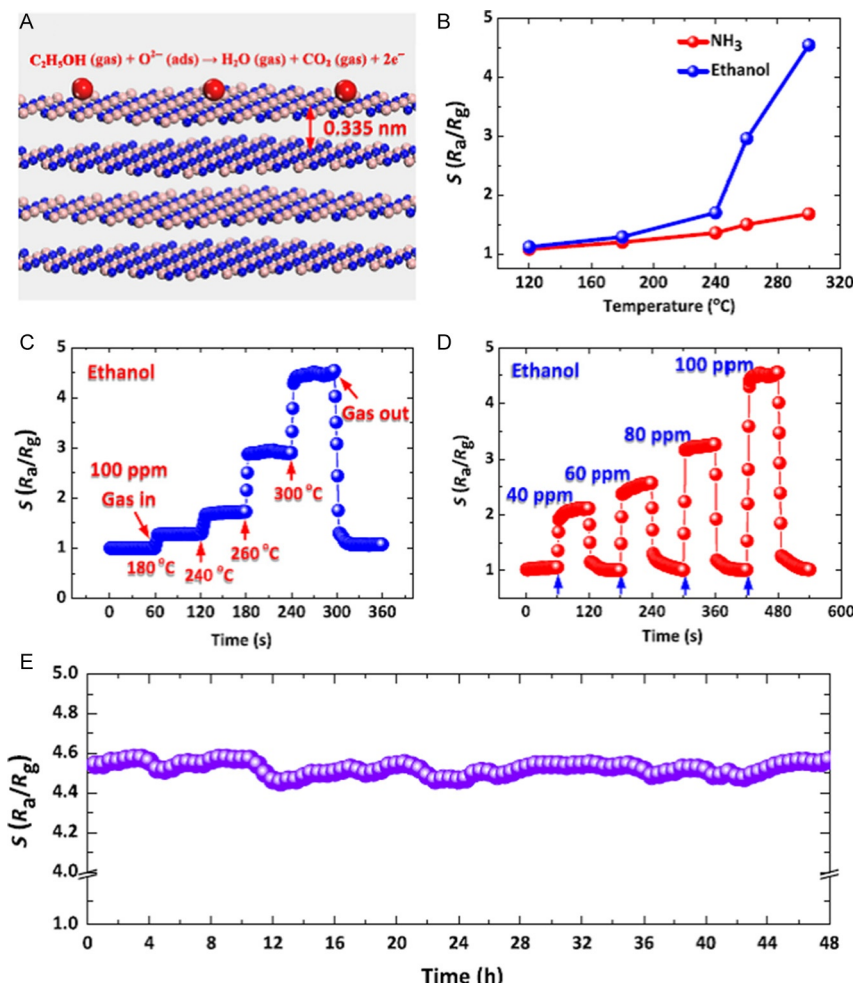


**Fig. 18** (A) Schematic showing the gas detection mechanism on the surface of the h-BN nanosheets. (B and C) Gas sensing for ammonia and ethanol at various temperatures. (D) Ethanol detection at various concentrations of gas input. (E) Change in the resistance over time (Lin et al., 2016).

desorption process of the oxygen molecules on the sensor surface. When the sensor is exposed to air, the oxygen molecules gets absorbed and are ionized by the available free electrons from the conduction band of the h-BN, resulting in an increase of the resistance. Similarly, when ethanol is introduced, it causes a reaction on the surface, which releases electrons back to the sensor, reducing the resistance. Hence, this mechanism is used to test the efficiency at various temperatures and concentrations of ethanol as observed in Fig. 18B–D. Although the sensitivity of this sensor is not as low as the traditional zinc oxide or tin oxide sensors, the response time is very short and is reproducible over a period of time (Fig. 18E), which still makes it a good gas sensor.

#### 4.5 h-BN as Filler for Binder-Free Anode for Lithium Ion Batteries

BNNSs were also used to make composite material with graphene oxide for binder-free anode for lithium ion battery application (Li et al., 2015a). The h-BN/rGO composite was first made via vacuum filtration (Fig. 19A),

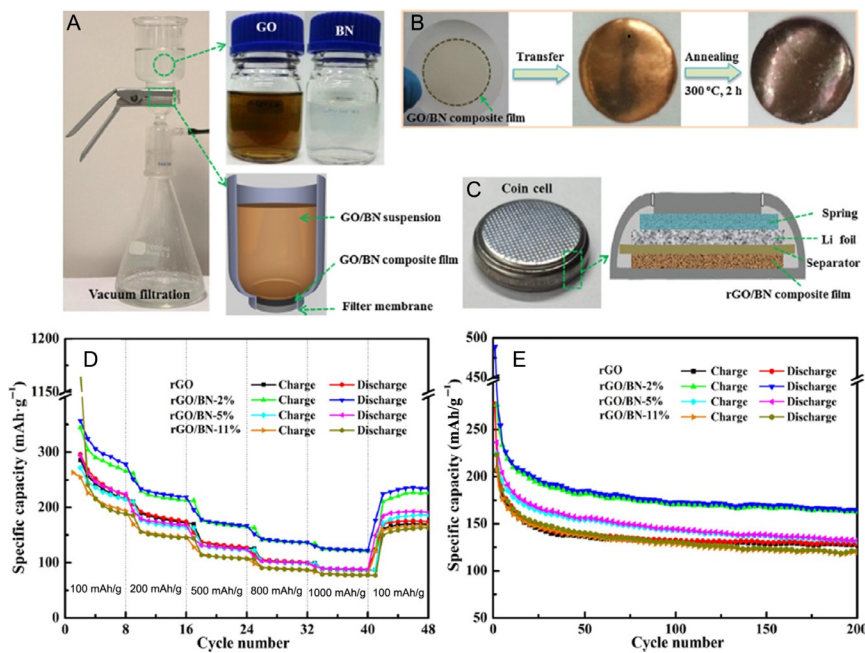


**Fig. 19** (A) Vacuum filtration process used to create the heterostructure of h-BN/GO. (B) Dried film obtained after the vacuum filtration which is transferred onto copper electrode. (C) Coin cell assembly structure with the h-BN/GO composite as anode and Li foil as cathode. (D) Rate performance for different current densities. (E) Cyclic performance of the composite showed a constant cycling capacity of 200 mAh/g (Li et al., 2015a).

which was then dried to form a film as observed in Fig. 19B, transferred onto a copper metal, and then annealed at 300°C for 24 h (Fig. 19C), which formed the anode material. This is placed against a lithium foil as cathode and a coin cell was made to test the performance of this heterostructure.

Varying concentrations of h-BN was tested to understand the effect of BN on the electrochemical performances of the coin cell as observed in Fig. 19D and E. This composite exhibited a high reversible cyclic capacity of 278 mAh/g at a high current density of 100 mA/g. It also exhibited a high rate capability and excellent cyclic stability and showed no obvious signs of decay even after 200 cycles. This is attributed to the synergistic effect between the rGO and the h-BN nanosheets. This addition of h-BN showed a way to improve on the fabrication of other graphene-based composite films for high-performance energy storage devices without the use of binders or additives.

## 4.6 Hyperbolicity in h-BN

Previously, graphene was shown to be an ideal material for tunable plasmonics in the mid-infrared and terahertz range because of the electrostatic doping and its ability to produce higher confinement and low loss when compared to metals. Similar to graphene, h-BN possesses extremely high confinement and even lower low loss (Caldwell et al., 2014; Cortes et al., 2014; Dai et al., 2015a). Also, h-BN is a natural hyperbolic material which can be used for its photonic properties such as spontaneous emission enhancement, negative refraction, and thermal radiation enhancement (Caldwell et al., 2015, 2016; Dai et al., 2015b; Gilburd et al., 2016; Ju et al., 2014; Kumar et al., 2015; Li et al., 2015b; Woessner et al., 2015). Hence, making a heterostructure with graphene–h-BN will allow the use of the electrical tenability and high quality through the hybrid plasmon–phonon polaritons. h-BN being a hyperbolic material, has one of the relative permittivity tensor's opposite to the other two components. This property leads to indefinite dispersion for electromagnetic waves to propagate inside the material, resulting in photonic properties. Hence, h-BN would act as an atomic scale hyperbolic metamaterials. It also has both type I and II hyperbolic responses in different spectra bands, which allows a direct comparison between them. Typically, this optical property determination is performed using a near-field optical microscopy combined with an infrared nanospectroscopy, as represented in Fig. 20A. The broadband nano-infrared spectra of the normalized scattering amplitude plotted as a

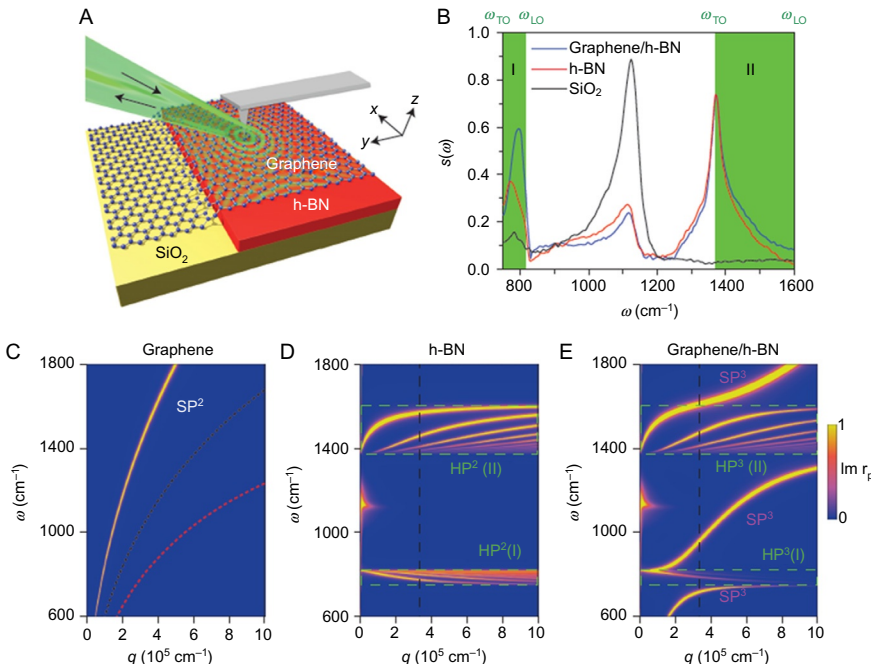


**Fig. 20** (A) Schematic showing the infrared beams from a monochromatic broadband laser which are incident on an AFM tip and backscattered light collected for extraction of near-field signal. (B) Broadband nano-infrared spectra of the metastructure with hBN thickness of 58 nm. (C) Calculated dispersion of the SPP ( $SP^2$ ) in freestanding graphene with Fermi energies of  $EF = 0.37, 0.15$ , and  $0.08$  eV. (D) Calculated dispersion of the hyperbolic phonon polaritons ( $HP^2$ ) in h-BN of thickness 58 nm. (E) Similar to (D) but for a graphene/h-BN structure with  $EF = 0.37$  eV. The false-color map reveals the dispersion of the hyperbolic plasmon–phonon polaritons ( $HP^3$ ) and the surface plasmon–phonon polaritons ( $SP^3$ ). Weak resonances around  $\omega = 1130$  cm<sup>-1</sup> in (D) and (E) originate from the SiO<sub>2</sub> substrate (Dai et al., 2015b).

function of frequency is represented in Fig. 20B for h-BN, SiO<sub>2</sub> substrate, and the graphene/h-BN metastructure. The hyperbolic regions of h-BN are highlighted in Fig. 20B where the type I has a frequency range of 746–819 cm<sup>-1</sup> and the type II has a range at 1370–1610 cm<sup>-1</sup>. Both the types of the resonances are modified for the metastructure as it can be observed in Fig. 20B. The presence of graphene significantly enhanced and blue shifted by  $\sim 25$  cm<sup>-1</sup> compared to that of h-BN alone. The surface plasmon polaritons (SPP) as measured are plotted in Fig. 20C and D for graphene and h-BN alone on SiO<sub>2</sub>. As it can be observed that h-BN has multiple distinct branches which correspond to the quantized

HP<sup>2</sup> waveguide modes with a scalar potential oscillating across the h-BN with a different number of nodes. Similarly, we can observe new dispersion modes, ie, hyperbolic plasmon–phonon polaritons (HP<sup>3</sup>) which arise from the mixing of HP<sup>2</sup> and SPP from graphene/h-BN structure. The graphene influence is clearly observed in the blue shift of the HP<sup>3</sup> frequencies with respect to the HP<sup>2</sup>, with a negative shift for type II band and positive shift in type I. This arises from the polariton dispersion being negative and positive in type I and type II regions. Hence, we can say that van der Waal polaritonic heterostructures with locally tunable properties will fulfil the essential prerequisites for the transformation of 2D plasmonics. The hybridization and graphene-induced tunability can be generic for most other electromagnetic materials and van der Waal's heterostructures.

Where only a few sets of applications were touched upon in this section, there are many potential exciting opportunities for ultrathin and 2D h-BN thin films. Coupled with the exciting material properties, the emergence of a greater understanding of nucleation and growth procedures, and continued push for 2D implantation into commercial devices, h-BN has a very promising future to directly impact many aspects of our daily lives for years to come.

## REFERENCES

- Alem, N., Erni, R., Kisielowski, C., Rossell, M., Gannett, W., Zettl, A., 2009. Atomically thin hexagonal boron nitride probed by ultrahigh-resolution transmission electron microscopy. *Phys. Rev. B* 80, 155425. <http://dx.doi.org/10.1103/PhysRevB.80.155425>.
- N. No, 1958. Manufacture of boron compounds, United States Patent Office, 2–4.
- Anota, E.C., Tlapale, Y., Villanueva, M.S., Márquez, J.A.R., 2015. Non-covalent functionalization of hexagonal boron nitride nanosheets with guanine. *J. Mol. Model.* 21, 215. <http://dx.doi.org/10.1007/s00894-015-2768-0>.
- Balmain, W.H., 1842. Bemerkungen über die Bildung von Verbindungen des Bors und Siliciums mit Stickstoff und gewissen Metallen. *Philos. Mag. J. Sci.* 62, 422–430. <http://dx.doi.org/10.1002/prac.18420270164>.
- Barth, J.V., Costantini, G., Kern, K., 2005. Engineering atomic and molecular nanostructures at surfaces. *Nature* 437, 671–679. <http://dx.doi.org/10.1038/nature04166>.
- Bhaviripudi, S., Jia, X., Dresselhaus, M.S., Kong, J., 2010. Role of kinetic factors in chemical vapor deposition synthesis of uniform large area graphene using copper catalyst. *Nano Lett.* 10, 4128–4133. <http://dx.doi.org/10.1021/nl102355e>.
- Bhimanapati, G.R., Kozuch, D., Robinson, J., 2014. Large-scale synthesis and functionalization of hexagonal boron nitride nanosheets. *Nanoscale* 6, 11671–11675. <http://dx.doi.org/10.1039/C4NR01816H>.
- Bhimanapati, G.R., Lin, Z., Meunier, V., Jung, Y., Cha, J.J., Das, S., et al., 2015. Recent advances in two-dimensional materials beyond graphene. *ACS Nano* 9, 11509–11539. <http://dx.doi.org/10.1021/acsnano.5b05556>.

- Blake, P., Hill, E.W., 2007. Making graphene visible. *Appl. Phys. Lett.* 91, 063124. <http://dx.doi.org/10.1063/1.2768624>.
- Boilotin, K.I., Sikes, K.J., Hone, J., Stormer, H.L., Kim, P., 2008. Temperature-dependent transport in suspended graphene. *Phys. Rev. Lett.* 101, 096802. <http://dx.doi.org/10.1103/PhysRevLett.101.096802>.
- Boucart, K., Ionescu, A.M., 2008. A new definition of threshold voltage in Tunnel FETs. *Solid State Electron.* 52, 1318–1323. <http://dx.doi.org/10.1016/j.sse.2008.04.003>.
- Bresnahan, M., Hollander, M.J., Wetherington, M.T., Wang, K., Miyagi, T., Pastor, G., et al., 2013. Prospects of direct growth boron nitride films as substrates for graphene electronics. *J. Mater. Res.* 29, 1–13. <http://dx.doi.org/10.1557/jmr.2013.323>.
- Bresnahan, M.S., Bhimanapati, G.R., Wang, K., Snyder, D.W., Robinson, J.A., 2014. Impact of copper overpressure on the synthesis of hexagonal boron nitride atomic layers. *ACS Appl. Mater. Interfaces* 6, 16755–16762. <http://dx.doi.org/10.1021/am503844u>.
- Britnell, L., Gorbachev, R.V., Jalil, R., Belle, B.D., Schedin, F., Katsnelson, M.I., et al., 2012. Electron tunneling through ultrathin boron nitride crystalline barriers. *Nano Lett.* 12, 1707–1710. <http://dx.doi.org/10.1021/nl3002205>.
- Bumm, L.A., Arnold, J.J., Dunbar, T.D., Allara, D.L., Weiss, P.S., 1999. Electron transfer through organic molecules. *J. Phys. Chem. B* 103, 8122–8127. <http://dx.doi.org/10.1021/jp9921699>.
- Bundy, F.P., 1963. Direct conversion of graphite to diamond in static pressure apparatus. *J. Chem. Phys.* 38, 631. <http://dx.doi.org/10.1063/1.1733716>.
- Caldwell, J.D., Kretinin, A., Chen, Y., Giannini, V., Fogler, M.M., Francescato, Y., et al., 2014. Sub-diffraction, volume-confined polaritons in the natural hyperbolic material, hexagonal boron nitride. *Nat. Commun.* 5, 1–9. <http://dx.doi.org/10.1038/ncomms6221>.
- Caldwell, J.D., Vurgaftman, I., Tischler, J.G., 2015. Probing hyperbolic polaritons. *Nat. Publ. Gr.* 9, 638–640. <http://dx.doi.org/10.1038/nphoton.2015.183>.
- Caldwell, J.D., Vurgaftman, I., Tischler, J.G., Glenbocki, O.J., Owrusky, J.C., Reinecke, T.L., 2016. Atomic-scale photonic hybrids for mid-infrared and terahertz nanophotonics. *Nat. Publ. Gr.* 11, 9–15. <http://dx.doi.org/10.1038/nnano.2015.305>.
- Chen, H., Zhang, H., Fu, L., Chen, Y., Williams, J.S., Yu, C., et al., 2008a. Nano Au-decorated boron nitride nanotubes: conductance modification and field-emission enhancement. *Appl. Phys. Lett.* 92, 243105. <http://dx.doi.org/10.1063/1.2943653>.
- Chen, J.-H., Jang, C., Xiao, S., Ishigami, M., Fuhrer, M.S., 2008b. Intrinsic and extrinsic performance limits of graphene devices on SiO<sub>2</sub>. *Nat. Nanotechnol.* 3, 206–209. <http://dx.doi.org/10.1038/nnano.2008.58>.
- Chen, X., Dobson, J.F., Raston, C.L., 2012. Vortex fluidic exfoliation of graphite and boron nitride. *Chem. Commun.* 48, 3703. <http://dx.doi.org/10.1039/c2cc17611d>.
- Cho, H., Park, S., Won, D.-I., Kang, S.O., Pyo, S.-S., Kim, D.-I., et al., 2015. Growth kinetics of white graphene (h-BN) on a planarised Ni foil surface. *Sci. Rep.* 5, 11985. <http://dx.doi.org/10.1038/srep11985>.
- Coleman, J.N., Lotya, M., O'Neill, A., Bergin, S.D., King, P.J., Khan, U., et al., 2011. Two-dimensional nanosheets produced by liquid exfoliation of layered materials. *Science* 331, 568–571. <http://dx.doi.org/10.1126/science.1194975>.
- Constantinescu, G., Kuc, A., Heine, T., 2013. Stacking in bulk and bilayer hexagonal boron nitride. *Phys. Rev. Lett.* 111, 036104. <http://dx.doi.org/10.1103/PhysRevLett.111.036104>.
- Corso, M., Auwärter, W., Muntwiler, M., Tamai, A., Greber, T., Osterwalder, J., 2004. Boron nitride nanomesh. *Science* 303, 217–220. <http://dx.doi.org/10.1126/science.1091979>.
- Cortes, C.L., Newman, W., Molesky, S., Jacob, Z., 2014. Corrigendum: quantum nanophotonics using hyperbolic metamaterials (2012 *J. Opt.* 14063001). *J. Opt.* 16, 129501. <http://dx.doi.org/10.1088/2040-8978/16/12/129501>.

- Cui, Y., Kim, S.N., Jones, S.E., Wissler, L.L., Naik, R.R., McAlpine, M.C., 2010. Chemical functionalization of graphene enabled by phage displayed peptides. *Nano Lett.* 10, 4559–4565. <http://dx.doi.org/10.1021/nl102564d>.
- Cui, Z., Oyer, A.J., Glover, A.J., Schniepp, H.C., Adamson, D.H., 2014. Large scale thermal exfoliation and functionalization of boron nitride. *Small* 10, 2352–2355. <http://dx.doi.org/10.1002/smll.201303236>.
- Dai, S., Ma, Q., Andersen, T., Mcleod, A.S., Fei, Z., Liu, M.K., et al., 2015a. Sub-diffractive focusing and guiding of polaritonic rays in a natural hyperbolic material. *Nat. Commun.* 6, 6963. <http://dx.doi.org/10.1038/ncomms7963>.
- Dai, S., Ma, Q., Liu, M.K., Andersen, T., Fei, Z., Gold, M.D., et al., 2015b. Graphene on hexagonal boron nitride as a tunable hyperbolic metamaterial. *Nat. Nanotechnol.* 10, 682–686. <http://dx.doi.org/10.1038/nnano.2015.131>.
- Dean, C.R., Young, A.F., Meric, I., Lee, C., Wang, L., Sorgenfrei, S., et al., 2010. Boron nitride substrates for high-quality graphene electronics. *Nat. Nanotechnol.* 5, 722–726. <http://dx.doi.org/10.1038/nnano.2010.172>.
- Dean, C., Young, A.F., Wang, L., Meric, I., Lee, G.H., Watanabe, K., et al., 2012. Graphene based heterostructures. *Solid State Commun.* 152, 1275–1282. <http://dx.doi.org/10.1016/j.ssc.2012.04.021>.
- Deepika, Li, L.H., Glushenkov, A.M., Hait, S.K., Hodgson, P., Chen, Y., 2014. High-efficient production of boron nitride nanosheets via an optimized ball milling process for lubrication in oil. *Sci. Rep.* 4, 7288. <http://dx.doi.org/10.1038/srep07288>.
- Ding, N., Chen, X., Wu, C.-M.L., Li, H., 2013. Adsorption of nucleobase pairs on hexagonal boron nitride sheet: hydrogen bonding versus stacking. *Phys. Chem. Chem. Phys.* 15, 10767–10776. <http://dx.doi.org/10.1039/c3cp50912e>.
- Erickson, K.J., Gibb, A.L., Sinitkii, A., Rousseas, M., Alem, N., Tour, J.M., et al., 2011. Longitudinal splitting of boron nitride nanotubes for the facile synthesis of high quality boron nitride nanoribbons. *Nano Lett.* 11, 3221–3226.
- Gannett, W., Regan, W., Watanabe, K., Taniguchi, T., Crommie, M.F., Zettl, A., 2011. Boron nitride substrates for high mobility chemical vapor deposited graphene. *Appl. Phys. Lett.* 98, 242105. <http://dx.doi.org/10.1063/1.3599708>.
- Gao, Z., Zhi, C., Golberg, D., Bando, Y., Serizawa, T., 2014. Noncovalent functionalization of boron nitride nanotubes in aqueous media. *Nanobiomedicine* 1, 1–14. <http://dx.doi.org/10.5772/60000>.
- Geim, A.K., Grigorieva, I.V., 2013. Van der Waals heterostructures. *Nature* 499, 419–425. <http://dx.doi.org/10.1038/nature12385>.
- Ghosh, J., Mazumdar, S., Das, M., Ghatak, S., Basu, A.K., 2008. Microstructural characterization of amorphous and nanocrystalline boron nitride prepared by high-energy ball milling. *Mater. Res. Bull.* 43, 1023–1031. <http://dx.doi.org/10.1016/j.materresbull.2007.04.022>.
- Gilburd, L., Xu, X.G., Bando, Y., Golberg, D., Walker, G.C., 2016. Near-field infrared pump-probe imaging of surface phonon coupling in boron nitride nanotubes. *J. Phys. Chem. Lett.* 7 (2), 289–294. <http://dx.doi.org/10.1021/acs.jpclett.5b02438>.
- Glavin, N.R., Jespersen, M.L., Check, M.H., Hu, J., Hilton, A.M., Fisher, T.S., et al., 2014. Synthesis of few-layer, large area hexagonal-boron nitride by pulsed laser deposition. *Thin Solid Films* 572, 245–250. <http://dx.doi.org/10.1016/j.tsf.2014.07.059>.
- Golberg, D., Bando, Y., Huang, Y., Terao, T., Mitome, M., Tang, C., et al., 2010. Boron nitride nanotubes and nanosheets. *ACS Nano* 4, 2979–2993. <http://dx.doi.org/10.1021/nn1006495>.
- Gorbachev, R.V., Riaz, I., Nair, R.R., Jalil, R., Britnell, L., Belle, B.D., et al., 2011. Hunting for monolayer boron nitride: optical and Raman signatures. *Small* 7, 465–468. <http://dx.doi.org/10.1002/smll.201001628>.
- Goriachko, A., He, Y., Knapp, M., Over, H., Corso, M., Brugger, T., et al., 2007. Self-assembly of a hexagonal boron nitride nanomesh on Ru(0001). *Langmuir* 23, 2928–2931. <http://dx.doi.org/10.1021/la062990t>.

- Grimme, S., 2011. Density functional theory with London dispersion corrections. *WIREs Comput. Mol. Sci.* 1, 211–228. <http://dx.doi.org/10.1002/wcms.30>.
- Grimme, S., Muck-Lichtenfeld, C., Antony, J., 2007. Noncovalent interactions between graphene sheets and in multishell (hyper)fullerenes. *J. Phys. Chem. C* 111, 11199–11207. <http://dx.doi.org/10.1021/jp0720791>.
- Han, W.-Q., Wu, L., Zhu, Y., Watanabe, K., Taniguchi, T., 2008. Structure of chemically derived mono- and few-atomic-layer boron nitride sheets. *Appl. Phys. Lett.* 93, 223103. <http://dx.doi.org/10.1063/1.3041639>.
- Hod, O., 2012. Graphite and hexagonal boron-nitride have the same interlayer distance. Why? *J. Chem. Theory Comput.* 8, 1360–1369. <http://dx.doi.org/10.1021/ct20080m>.
- Hua Li, L., Chen, Y., Cheng, B.M., Lin, M.Y., Chou, S.L., Peng, Y.C., 2012. Photoluminescence of boron nitride nanosheets exfoliated by ball milling. *Appl. Phys. Lett.* 100, 261108. <http://dx.doi.org/10.1063/1.4731203>.
- Jacobson, N., Farmer, S., Moore, A., Sayir, H., 1999. High-temperature oxidation of boron nitride: I. Monolithic boron nitride. *J. Am. Ceram. Soc.* 82, 393–398. <http://dx.doi.org/10.1111/j.1151-2916.1999.tb01944.x>.
- Jiang, J.W., Wang, J.S., Li, B., 2009. Thermal conductance of graphene and dimerite. *Phys. Rev. B* 79, 205418. <http://dx.doi.org/10.1103/PhysRevB.79.205418>.
- Jin, C., Lin, F., Suenaga, K., Iijima, S., 2009. Fabrication of a freestanding boron nitride single layer and its defect assignments. *Phys. Rev. Lett.* 102, 3–6. <http://dx.doi.org/10.1103/PhysRevLett.102.195505>.
- Ju, L., Jr, J.V., Huang, E., Kahn, S., Nosiglia, C., Tsai, H., et al., 2014. Photoinduced doping in heterostructures of graphene and boron nitride. *Nat. Nanotechnol.* 9, 348–352. <http://dx.doi.org/10.1038/nnano.2014.60>.
- Kim, K.K., Hsu, A., Jia, X., Kim, S.M., Shi, Y., Hofmann, M., et al., 2012a. Synthesis of monolayer hexagonal boron nitride on Cu foil using chemical vapor deposition. *Nano Lett.* 12, 161–166. <http://dx.doi.org/10.1021/nl203249a>.
- Kim, K.K., Hsu, A., Jia, X., Kim, S.M., Shi, Y., Dresselhaus, M., et al., 2012b. Synthesis and characterization of hexagonal boron nitride film as a dielectric layer for graphene devices. *ACS Nano* 6, 8583–8590. <http://dx.doi.org/10.1021/nn301675f>.
- Kim, G., Jang, A.-R., Jeong, H.Y., Lee, Z., Kang, D.J., Shin, H.S., 2013. Growth of high-crystalline, single-layer hexagonal boron nitride on recyclable platinum foil. *Nano Lett.* 13, 1834–1839. <http://dx.doi.org/10.1021/nl400559s>.
- Kosynkin, D.V., Lu, W., Sinitskii, A., Pera, G., Sun, Z., Tour, J.M., 2011. Highly conductive graphene nanoribbons by longitudinal splitting of carbon nanotubes using potassium vapor. *ACS Nano* 5, 968–974. <http://dx.doi.org/10.1021/nn102326c>.
- Kuila, T., Bose, S., Mishra, A.K., Khanra, P., Kim, N.H., Lee, J.H., 2012. Chemical functionalization of graphene and its applications. *Prog. Mater. Sci.* 57, 1061–1105. <http://dx.doi.org/10.1016/j.pmatsci.2012.03.002>.
- Kumar, A., Low, T., Fung, K.H., Avouris, P., Fang, N.X., 2015. Tunable light–matter interaction and the role of hyperbolicity in graphene–hBN system. *Nano Lett.* 15, 3172–3180. <http://dx.doi.org/10.1021/acs.nanolett.5b01191>.
- Lan, J., Wang, J.-S., Gan, C.K., Chin, S.K., 2009. Edge effects on quantum thermal transport in graphene nanoribbons: tight-binding calculations. *Phys. Rev. B* 79, 115401. <http://dx.doi.org/10.1103/PhysRevB.79.115401>.
- Lee, C., Li, Q., Kalb, W., Liu, X.-Z., Berger, H., Carpick, R.W., et al., 2010. Frictional characteristics of atomically thin sheets. *Science* 328, 76–80. <http://dx.doi.org/10.1126/science.1184167>.
- Lee, G.-H., Yu, Y.-J., Lee, C., Dean, C., Shepard, K.L., Kim, P., et al., 2011. Electron tunneling through atomically flat and ultrathin hexagonal boron nitride. *Appl. Phys. Lett.* 99, 243114. <http://dx.doi.org/10.1063/1.3662043>.

- Lee, Y.-H., Liu, K.-K., Lu, A.-Y., Wu, C.-Y., Lin, C.-T., Zhang, W., et al., 2012a. Growth selectivity of hexagonal-boron nitride layers on Ni with various crystal orientations. *RSC Adv.* 2, 111. <http://dx.doi.org/10.1039/c1ra00703c>.
- Lee, K.H., Shin, H.J., Lee, J., Lee, I.Y., Kim, G.H., Choi, J.Y., et al., 2012b. Large-scale synthesis of high-quality hexagonal boron nitride nanosheets for large-area graphene electronics. *Nano Lett.* 12, 714–718. <http://dx.doi.org/10.1021/nl203635v>.
- Lee, G.H., Yu, Y.J., Cui, X., Petrone, N., Lee, C.H., Choi, M.S., et al., 2013. Flexible and transparent MoS<sub>2</sub> field-effect transistors on hexagonal boron nitride-graphene heterostructures. *ACS Nano* 7, 7931–7936. <http://dx.doi.org/10.1021/nn402954e>.
- Lee, D., Lee, B., Park, K.H., Ryu, H.J., Jeon, S., Hong, S.H., 2015. Scalable exfoliation process for highly soluble boron nitride nanoplatelets by hydroxide-assisted ball milling. *Nano Lett.* 15, 1238–1244. <http://dx.doi.org/10.1021/nl504397h>.
- Li, L.H., Chen, Y., Behan, G., Zhang, H., Petracic, M., Glushenkov, A.M., 2011. Large-scale mechanical peeling of boron nitride nanosheets by low-energy ball milling. *J. Mater. Chem.* 21, 11862. <http://dx.doi.org/10.1039/c1jm11192b>.
- Li, X., Hao, X., Zhao, M., Wu, Y., Yang, J., Tian, Y., et al., 2013. Exfoliation of hexagonal boron nitride by molten hydroxides. *Adv. Mater.* 25, 2200–2204. <http://dx.doi.org/10.1002/adma.201204031>.
- Li, H., Tay, R.Y., Tsang, S.H., Liu, W., Teo, E.H.T., 2015a. Reduced graphene oxide/boron nitride composite film as a novel binder-free anode for lithium ion batteries with enhanced performances. *Electrochim. Acta* 166, 197–205. <http://dx.doi.org/10.1016/j.electacta.2015.03.109>.
- Li, P., Lewin, M., Kretinin, A.V., Caldwell, J.D., Novoselov, K.S., Taniguchi, T., et al., 2015b. Hyperbolic phonon-polaritons in boron nitride for near-field optical imaging and focusing. *Nat. Commun.* 6, 1–9. <http://dx.doi.org/10.1038/ncomms8507>.
- Liao, L., Lin, Y.-C., Bao, M., Cheng, R., Bai, J., Liu, Y., et al., 2010. High-speed graphene transistors with a self-aligned nanowire gate. *Nature* 467, 305–308. <http://dx.doi.org/10.1038/nature09405>.
- Lin, Y., Connell, J.W., 2012. Advances in 2D boron nitride nanostructures: nanosheets, nanoribbons, nanomeshes, and hybrids with graphene. *Nanoscale* 4, 6908. <http://dx.doi.org/10.1039/c2nr32201c>.
- Lin, Y., Williams, T.V., Connell, J.W., 2010a. Soluble, exfoliated hexagonal boron nitride nanosheets. *J. Phys. Chem. Lett.* 1, 277–283. <http://dx.doi.org/10.1021/jz9002108>.
- Lin, Y., Williams, T.V., Cao, W., Elsayed-Ali, H.E., Connell, J.W., 2010b. Defect functionalization of hexagonal boron nitride nanosheets. *J. Phys. Chem. C* 114, 17434–17439. <http://dx.doi.org/10.1021/jp105454w>.
- Lin, Y.-M., Dimitrakopoulos, C., Jenkins, K.A., Farmer, D.B., Chiu, H.-Y., Grill, A., et al., 2010c. 100-GHz transistors from wafer-scale epitaxial graphene. *Science* 327, 662. <http://dx.doi.org/10.1126/science.1184289>.
- Lin, Y., Williams, T.V., Xu, T.-B., Cao, W., Elsayed-Ali, H.E., Connell, J.W., 2011a. Aqueous dispersions of few-layered and monolayered hexagonal boron nitride nanosheets from sonication-assisted hydrolysis: critical role of water. *J. Phys. Chem. C* 115, 2679–2685. <http://dx.doi.org/10.1021/jp110985w>.
- Lin, Q., Zou, X., Zhou, G., Liu, R., Wu, J., Li, J., et al., 2011b. Adsorption of DNA/RNA nucleobases on hexagonal boron nitride sheet: an ab initio study. *Phys. Chem. Chem. Phys.* 13, 12225–12230. <http://dx.doi.org/10.1039/c1cp20783k>.
- Lin, L., Liu, T., Zhang, Y., Sun, R., Zeng, W., Wang, Z., 2016. Synthesis of boron nitride nanosheets with a few atomic layers and their gas-sensing performance. *Ceram. Int.* 42, 971–975. <http://dx.doi.org/10.1016/j.ceramint.2015.08.109>.
- Liu, Y., Bhowmick, S., Yakobson, B.I., 2011. BN white graphene with “colorful” edges: the energies and morphology. *Nano Lett.* 11, 3113–3116. <http://dx.doi.org/10.1021/nl2011142>.

- Liu, Z., Gong, Y., Zhou, W., Ma, L., Yu, J., Idrobo, J.C., et al., 2013. Ultrathin high-temperature oxidation-resistant coatings of hexagonal boron nitride. *Nat. Commun.* 4, 1–8. <http://dx.doi.org/10.1038/ncomms3541>.
- Liu, G., Rumyantsev, S.L., Jiang, C., Shur, M.S., Balandin, A.A., 2015. Gas sensing with h-BN capped MoS<sub>2</sub> heterostructure thin film transistors. *IEEE Electron Device Lett.* 36, 1202–1204.
- Lu, G., Wu, T., Yuan, Q., Wang, H., Wang, H., Ding, F., et al., 2015. Synthesis of large single-crystal hexagonal boron nitride grains on Cu–Ni alloy. *Nat. Commun.* 6, 6160. <http://dx.doi.org/10.1038/ncomms7160>.
- Marom, N., Bernstein, J., Garel, J., Tkatchenko, A., Joselevich, E., Kronik, L., et al., 2010. Stacking and registry effects in layered materials: the case of hexagonal boron nitride. *Phys. Rev. Lett.* 105, 046801. <http://dx.doi.org/10.1103/PhysRevLett.105.046801>.
- Martin, J., Akerman, N., Ulbricht, G., Lohmann, T., Smet, J.H., von Klitzing, K., et al., 2008. Observation of electron–hole puddles in graphene using a scanning single-electron transistor. *Nat. Phys.* 4, 144–148. <http://dx.doi.org/10.1038/nphys781>.
- Meyer, J.C., Chuvilin, A., Algara-Siller, G., Biskupek, J., Kaiser, U., 2009. Selective sputtering and atomic resolution imaging of atomically thin boron nitride membranes. *Nano Lett.* 9, 2683–2689. <http://dx.doi.org/10.1021/nl9011497>.
- Moore, A.W., Duclaux, L., Nysten, B., Issi, J.-P., 1992. Structure and low temperature thermal conductivity of pyrolytic boron nitride. *Phys. Rev. B* 46, 3362.
- Morozov, S.V., Novoselov, K.S., Katsnelson, M.I., Schedin, F., Elias, D.C., Jaszzak, J.A., et al., 2008. Giant intrinsic carrier mobilities in graphene and its bilayer. *Phys. Rev. Lett.* 100, 11–14. <http://dx.doi.org/10.1103/PhysRevLett.100.016602>.
- Morscher, M., Corso, M., Greber, T., Osterwalder, J., 2006. Formation of single layer h-BN on Pd(1 1 1). *Surf. Sci.* 600, 3280–3284. <http://dx.doi.org/10.1016/j.susc.2006.06.016>.
- Nagashima, A., Tejima, N., Gamou, Y., Kawai, T., Oshima, C., 1996. Electronic states of monolayer hexagonal boron nitride formed on the metal surfaces. *Surf. Sci.* 357–358, 307–311. [http://dx.doi.org/10.1016/0039-6028\(96\)00134-3](http://dx.doi.org/10.1016/0039-6028(96)00134-3).
- Nakhaie, S., Wofford, J.M., Schumann, T., Jahn, U., Ramsteiner, M., Hanke, M., et al., 2015. Synthesis of atomically thin hexagonal boron nitride films on nickel foils by molecular beam epitaxy. *Appl. Phys. Lett.* 106, 213108. <http://dx.doi.org/10.1063/1.4921921>.
- Nayfeh, O.M., Glen Birdwell, A., Tan, C., Dubey, M., Gullapalli, H., Liu, Z., et al., 2013. Increased mobility for layer-by-layer transferred chemical vapor deposited graphene/boron-nitride thin films. *Appl. Phys. Lett.* 102, 103115. <http://dx.doi.org/10.1063/1.4794533>.
- Novoselov, K.S., Geim, A.K., Morozov, S.V., Jiang, D., Zhang, Y., Dubonos, S.V., et al., 2004. Electric field effect in atomically thin carbon films. *Science* 306, 666–669. <http://dx.doi.org/10.1126/science.1102896>.
- Novoselov, K.S., Jiang, D., Schedin, F., Booth, T.J., Khotkevich, V.V., Morozov, S.V., et al., 2005. Two-dimensional atomic crystals. *Proc. Natl. Acad. Sci. U.S.A.* 102, 10451–10453. <http://dx.doi.org/10.1073/pnas.0502848102>.
- Okada, S., Otani, M., 2010. Stability and electronic structure of potassium-intercalated hexagonal boron nitride from density functional calculations. *Phys. Rev. B* 81, 3–6. <http://dx.doi.org/10.1103/PhysRevB.81.233401>.
- Oliveira, C.K., Matos, M.J.S., Mazzoni, M.S.C., Chacham, H., Neves, B.R.A., 2012. Anomalous response of supported few-layer hexagonal boron nitride to DC electric fields: a confined water effect? *Nanotechnology* 23, 175703. <http://dx.doi.org/10.1088/0957-4484/23/17/175703>.
- Osada, M., Sasaki, T., 2012. Two-dimensional dielectric nanosheets: novel nanoelectronics from nanocrystal building blocks. *Adv. Mater.* 24, 210–228. <http://dx.doi.org/10.1002/adma.201103241>.

- Ouyang, T., Chen, Y., Xie, Y., Yang, K., Bao, Z., Zhong, J., 2010. Thermal transport in hexagonal boron nitride nanoribbons. *Nanotechnology* 21, 245701. <http://dx.doi.org/10.1088/0957-4484/21/24/245701>.
- Pacilé, D., Meyer, J.C., Girit, C.O., Zettl, A., 2008. The two-dimensional phase of boron nitride: few-atomic-layer sheets and suspended membranes. *Appl. Phys. Lett.* 92, 133107. <http://dx.doi.org/10.1063/1.2903702>.
- Paine, R., Narula, C., 1990. Synthetic routes to boron nitride. *Chem. Rev.* 90, 73–91. <http://pubs.acs.org/doi/abs/10.1021/cr00099a004> (accessed February 19, 2014).
- Pakdel, A., Bando, Y., Golberg, D., 2014. Nano boron nitride flatland. *Chem. Soc. Rev.* 43, 934–959. <http://dx.doi.org/10.1039/c3cs60260e>.
- Paton, K.R., Varrla, E., Backes, C., Smith, R.J., Khan, U., O'Neill, A., et al., 2014. Scalable production of large quantities of defect-free few-layer graphene by shear exfoliation in liquids. *Nat. Mater.* 13, 624–630. <http://dx.doi.org/10.1038/nmat3944>.
- Postole, G., Calderaru, M., Ionescu, N.I., Bonnetot, B., Auroux, A., Guimon, C., 2005. Boron nitride: a high potential support for combustion catalysts. *Thermochim. Acta* 434, 150–157. <http://dx.doi.org/10.1016/j.tca.2005.01.007>.
- Preobrajenski, A.B., Vinogradov, A.S., Mårtensson, N., 2005. Monolayer of h-BN chemisorbed on Cu(111) and Ni(111): the role of the transition metal 3d states. *Surf. Sci.* 582, 21–30. <http://dx.doi.org/10.1016/j.susc.2005.02.047>.
- Rafiee, M.A., Narayanan, T.N., Hashim, D.P., Sakhavand, N., Shahsavari, R., Vajtai, R., et al., 2013. Hexagonal boron nitride and graphite oxide reinforced multifunctional porous cement composites. *Adv. Funct. Mater.* 23, 5624–5630. <http://dx.doi.org/10.1002/adfm.201203866>.
- Rokuta, E., Hasegawa, Y., Suzuki, K., Gamou, Y., Oshima, C., Nagashima, A., 1997. Phonon dispersion of an epitaxial monolayer film of hexagonal boron nitride on Ni(111). *Phys. Rev. Lett.* 79, 4609–4612. <http://dx.doi.org/10.1103/PhysRevLett.79.4609>.
- Roy, A.K., Park, B., Lee, K.S., Park, S.Y., In, I., 2014a. Boron nitride nanosheets decorated with silver nanoparticles through mussel-inspired chemistry of dopamine. *Nanotechnology* 25, 445603. <http://dx.doi.org/10.1088/0957-4484/25/44/445603>.
- Roy, T., Tosun, M., Kang, J.S., Sachid, A.B., Desai, S.B., Hettick, M., et al., 2014b. Field-effect transistors built from all two-dimensional material components. *ACS Nano* 8, 6259–6264. <http://dx.doi.org/10.1021/nn501723y>.
- Sainsbury, T., Satti, A., May, P., O'Neill, A., Nicolosi, V., Gun'Ko, Y.K., et al., 2012. Covalently functionalized hexagonal boron nitride nanosheets by nitrene addition. *Chem. Eur. J.* 18, 10808–10812. <http://dx.doi.org/10.1002/chem.201201734>.
- Sainsbury, T., O'Neill, A., Passarelli, M.K., Seraffon, M., Gohil, D., Gnaniah, S., et al., 2014. Dibromocarbene functionalization of boron nitride nanosheets: toward band gap manipulation and nanocomposite applications. *Chem. Mater.* 26, 7039–7050. <http://dx.doi.org/10.1021/cm503475t>. 141208064817004.
- Sajjad, M., Morell, G., Feng, P., 2013. Advance in novel boron nitride nanosheets to nanoelectronic device applications. *ACS Appl. Mater. Interfaces* 5, 8–13.
- Shen, J., He, Y., Wu, J., Gao, C., Keyshar, K., Zhang, X., et al., 2015. Liquid phase exfoliation of two-dimensional materials by directly probing and matching surface tension components. *Nano Lett.* 15, 5449–5454. <http://dx.doi.org/10.1021/acs.nanolett.5b01842>. 150724081634000.
- Shi, Y., Hamsen, C., Jia, X., Kim, K.K., Reina, A., Hofmann, M., et al., 2010. Synthesis of few-layer hexagonal boron nitride thin film by chemical vapor deposition. *Nano Lett.* 10, 4134–4139. <http://dx.doi.org/10.1021/nl1023707>.
- Sinclair, W., Simmons, H., 1987. Microstructure and thermal shock behaviour of BN composites. *J. Mater. Sci. Lett.* 6, 627–629.
- Solozhenko, V.L., Turkevich, V.Z., Holzapfel, W.B., 1999. Refined phase diagram of boron nitride. *J. Phys. Chem. B* 103, 2903–2905. <http://dx.doi.org/10.1021/jp984682c>.

- Song, L., Ci, L., Lu, H., Sorokin, P.B., Jin, C., Ni, J., et al., 2010. Large scale growth and characterization of atomic hexagonal boron nitride layers. *Nano Lett.* 10, 3209–3215. <http://dx.doi.org/10.1021/nl1022139>.
- Song, W.-L., Wang, P., Cao, L., Anderson, A., Meziani, M.J., Farr, A.J., et al., 2012. Polymer/boron nitride nanocomposite materials for superior thermal transport performance. *Angew. Chem. Int. Ed. Engl.* 51, 6498–6501. <http://dx.doi.org/10.1002/anie.201201689>.
- Stehle, Y., Meyer, H.M., Unocic, R.R., Kidder, M., Polizos, G., Datskos, P.G., et al., 2015. Synthesis of hexagonal boron nitride monolayer: control of nucleation and crystal morphology. *Chem. Mater.* 27, 8041–8047. <http://dx.doi.org/10.1021/acs.chemmater.5b03607>.
- Sutter, P., Lahiri, J., Zahl, P., Wang, B., Sutter, E., 2013. Scalable synthesis of uniform few-layer hexagonal boron nitride dielectric films. *Nano Lett.* 13, 276–281. <http://dx.doi.org/10.1021/nl304080y>.
- Tang, S., Wang, H., Zhang, Y., Li, A., Xie, H., Liu, X., et al., 2013a. Precisely aligned graphene grown on hexagonal boron nitride by catalyst free chemical vapor deposition. *Sci. Rep.* 3, 1–7. <http://dx.doi.org/10.1038/srep02666>. <http://www.nature.com/srep/2013/130916/srep02666/abs/srep02666.html#supplementary-information>.
- Tang, S., Wang, H., Zhang, Y., Li, A., Xie, H., Liu, X., et al., 2013b. Precisely aligned graphene grown on hexagonal boron nitride by catalyst free chemical vapor deposition. *Sci. Rep.* 3, 1–7. <http://dx.doi.org/10.1038/srep02666>.
- Vlassiouk, I., Smirnov, S., Regmi, M., Surwade, S.P., Srivastava, N., Feenstra, R., et al., 2013. Graphene nucleation density on copper: fundamental role of background pressure. *J. Phys. Chem. C* 117, 18919–18926. <http://dx.doi.org/10.1021/jp4047648>.
- Wang, Y., Shi, Z., Yin, J., 2011a. Boron nitride nanosheets: large-scale exfoliation in methanesulfonic acid and their composites with polybenzimidazole. *J. Mater. Chem.* 21, 11371–11377. <http://dx.doi.org/10.1039/c1jm10342c>.
- Wang, H., Taychatanapat, T., Hsu, A., Watanabe, K., Taniguchi, T., Jarillo-herrero, P., et al., 2011b. BN/graphene/BN transistors for RF applications. *Nano* 32, 1209–1211.
- Warner, J.H., Rümmeli, M.H., Bachmatiuk, A., Büchner, B., 2010. Atomic resolution imaging and topography of boron nitride sheets produced by chemical exfoliation. *ACS Nano* 4, 1299–1304. <http://dx.doi.org/10.1021/nn901648q>.
- Watanabe, K., Taniguchi, T., Kanda, H., 2004. Direct-bandgap properties and evidence for ultraviolet lasing of hexagonal boron nitride single crystal. *Nat. Mater.* 3, 404–409. <http://dx.doi.org/10.1038/nmat1134>.
- Woessner, A., Lundeberg, M.B., Gao, Y., Principi, A., Alonso-gonzález, P., Carrega, M., et al., 2015. Highly confined low-loss plasmons in graphene–boron nitride heterostructures. *Nat. Mater.* 14, 421–425. <http://dx.doi.org/10.1038/NMAT4169>.
- Wong, D., Jr., J.V., Ju, L., Lee, J., Kahn, S., Tsai, H., et al., 2015. Characterization and manipulation of individual defects in insulating hexagonal boron nitride using scanning tunnelling microscopy. *Nat. Nanotechnol.* 10, 949–953. <http://dx.doi.org/10.1038/nnano.2015.188>.
- Xie, S.-Y., Wang, W., Fernando, K.A.S., Wang, X., Lin, Y., Sun, Y.-P., 2005. Solubilization of boron nitride nanotubes. *Chem. Commun. (Camb.)*, 3670–3672. <http://dx.doi.org/10.1039/b505330g>.
- Xu, Chao, Qiu, Xiaoqing, Huang, Caijin, Chen, Cheng, Ye, Xinxin, Ye, Weiqing, Hu, Jinli, 2013. Stable colloidal boron nitride nanosheet dispersion and its potential application in catalysis. *J. Mater. Chem. A* 1, 12192–12197. <http://dx.doi.org/10.1039/c3ta12231j>.
- Yang, Y., Fu, Q., Li, H., Wei, M., Xiao, J., Wei, W., et al., 2015. Creating a nanospace under an h-BN cover for adlayer growth on Nickel(111). *ACS Nano* 9, 11589–11598.

- Yao, Y., Lin, Z., Li, Z., Song, X., Moon, K.-S., Wong, C., 2012. Large-scale production of two-dimensional nanosheets. *J. Mater. Chem.* 22, 13494. <http://dx.doi.org/10.1039/c2jm30587a>.
- Yates, B., Overy, M.J., Pirgon, O., 1975. The anisotropic thermal expansion of boron nitride. 1. Experimental results and their analysis. *Philos. Mag.* 32, 847–857.
- Yin, J., Yu, J., Li, X., Li, J., Zhou, J., Zhang, Z., et al., 2015. Large single-crystal hexagonal boron nitride monolayer domains with controlled morphology and straight merging boundaries. *Small* 11, 4497–4502. <http://dx.doi.org/10.1002/smll.201500210>.
- Yu, J., Huang, X., Wu, C., Wu, X., Wang, G., Jiang, P., 2012. Interfacial modification of boron nitride nanoplatelets for epoxy composites with improved thermal properties. *Polymer* 53, 471–480. <http://dx.doi.org/10.1016/j.polymer.2011.12.040>.
- Yurdakul, H., Göncü, Y., Durukan, O., Akay, A., Seyhan, A.T., Ay, N., et al., 2012. Nanoscopic characterization of two-dimensional (2D) boron nitride nanosheets (BNNSS) produced by microfluidization. *Ceram. Int.* 38, 2187–2193. <http://dx.doi.org/10.1016/j.ceramint.2011.10.064>.
- Zeng, H., Zhi, C., Zhang, Z., Wei, X., Wang, X., Guo, W., et al., 2010. “White graphenes”: boron nitride nanoribbons via boron nitride nanotube unwrapping. *Nano Lett.* 10, 5049–5055. <http://dx.doi.org/10.1021/nl103251m>.
- Zeng, X., Ye, L., Yu, S., Li, H., Sun, R., Xu, J., et al., 2015. Artificial nacre-like papers based on noncovalent functionalized boron nitride nanosheets with excellent mechanical and thermally conductive properties. *Nanoscale* 7, 6774–6781. <http://dx.doi.org/10.1039/C5NR00228A>.
- Zhang, Y., Chang, T.-R., Zhou, B., Cui, Y.-T., Yan, H., Liu, Z., et al., 2014. Direct observation of the transition from indirect to direct bandgap in atomically thin epitaxial MoSe<sub>2</sub>. *Nat. Nanotechnol.* 9, 111–115. <http://dx.doi.org/10.1038/nnano.2013.277>.
- Zhi, C., Bando, Y., Tang, C., Golberg, D., Xie, R., Sekigushi, T., 2005. Phonon characteristics and cathodoluminescence of boron nitride nanotubes. *Appl. Phys. Lett.* 86, 213110. <http://dx.doi.org/10.1063/1.1938002>.
- Zhi, C., Bando, Y., Tang, C., Kuwahara, H., Golberg, D., 2009. Large-scale fabrication of boron nitride nanosheets and their utilization in polymeric composites with improved thermal and mechanical properties. *Adv. Mater.* 21, 2889–2893. <http://dx.doi.org/10.1002/adma.200900323>.